Transport of volcanic aerosol from the Raikoke eruption in 2019 through the Northern Hemisphere

Zhen Yang[1,2,3], Bärbel Vogel[1,3], Felix Plöger[1,3,12], Zhixuan Bai[2], Dan Li[4,2], Sabine Griessbach[5,3], Lars Hoffmann[5,3], Frank G. Wienhold[6], Elizabeth Asher[7,8], Alexandre A. Baron[7,9], Katie R. Smith[7,9], Troy Thornberry[9], Jianchun Bian[2,10,11], and Michaela I. Hegglin[1,3,12,13]

[1]Institute of Climate and Energy Systems: Stratosphere (ICE-4), Forschungszentrum Jülich, Jülich, Germany
[2]Laboratory of Middle Atmosphere and Global Environment Observation (LAGEO), Institute of Atmospheric Physics, Chinese Academy of Sciences, Beijing, China
[3]Centre for Advanced Simulation and Analytics (CASA), Forschungszentrum Jülich, Jülich, Germany
[4]State Key Laboratory of Atmospheric Environment and Extreme Meteorology, Institute of Atmospheric Physics, Chinese Academy of Sciences, Beijing, China
[5]Jülich Supercomputing Centre, Forschungszentrum Jülich, Jülich, Germany
[6]Institute for Atmospheric and Climate Science (IAC), ETH Zurich, Zurich, Switzerland
[7]Cooperative Institute for Research in Environmental Sciences (CIRES), University of Colorado Boulder, Boulder, CO, USA
[8]NOAA Global Monitoring Laboratory, Boulder, CO, USA
[9]NOAA Chemical Sciences Laboratory, Boulder, CO, USA
[10]College of Earth and Planetary Sciences, University of Chinese Academy of Sciences, Beijing, China
[11]College of Atmospheric Sciences, Lanzhou University, Lanzhou, China
[12]Institute for Atmospheric and Environmental Research, University of Wuppertal, Wuppertal, Germany
[13]Department of Meteorology, University of Reading, Reading, UK

Correspondence: Zhen Yang (yangzhen212121@gmail.com) and Bärbel Vogel (b.vogel@fz-juelich.de)

Abstract. Volcanic injections into the upper troposphere–lower stratosphere (UTLS) affect climate by altering Earth's radiation budget and atmospheric chemistry. However, the pathways by which mid-latitude eruptions spread globally remain poorly understood. We combine nighttime Compact Optical Backscatter Aerosol Detector (COBALD) profiles over Lhasa (China) with ERA5-driven Chemical Lagrangian Model of the Stratosphere (CLaMS) backward trajectories and global three-dimensional sulfur dioxide (SO_2)-based tracer simulations. With this integrated framework, we track the ~~Raikoke plume~~ plume of the Raikoke eruption (21–22 June 2019~~; VEI 4) as it evolved within~~) during its transport through the Northern Hemisphere and its interaction with the mature Asian Summer Monsoon Anticyclone (ASMA). Balloon-borne measurements capture the plume's arrival, vertical spreading, and dilution by ~~ASMA-interior air~~ air in the ASMA interior. Trajectories reveal two principal pathways from distinct Raikoke plumes: (i) an upper-level branch within the summertime stratospheric easterly flow ($\sim$ 460–490 K) carrying the trailing filament of the vorticized volcanic plume (VVP), and (ii) a lower-level branch within the subtropical westerly jet ($\sim$ 390–430 K) carrying the main plume. Although the ASMA can act as a transport barrier at certain potential-temperature levels, it admits ~~in-mixing~~ mixing into the anticyclone along jet-aligned filaments and redistributes aerosols internally. ~~SO_2-based tracer simulations are sensitive to how parameterized small-scale mixing is represented in CLaMS, underscoring the need to adjust subgrid-scale mixing parameterizations when model resolution changes (here, from ERA-Interim to ERA5 reanalyses). Independent~~ We show that the transport of the volcanic plume is sensitive to parameterized

mixing by varying the mixing strength in CLaMS. Portable Optical Particle Spectrometer (POPS) profiles over Boulder (USA) confirm the plume's timing and altitude, providing ~~out-of-region validation. Sensitivity to injection level indicates an additional ~ 4–5 km of uplift from aerosol-radiative lofting~~an independent evaluation of its transport outside the ASMA region.

1 Introduction

The impact of volcanic eruptions on climate has been a subject of widespread concern ~~(McCormick et al., 1995; Thompson and Solomon, 2~~(McCormick et al., 1995; Thompson and Solomon, 2009; Solomon et al., 2011; Bourassa et al., 2012; Masson-Delmotte et al., 2021; Schr. Large eruptions can inject significant amounts of ash ~~, water vapor,~~ and sulfur dioxide (SO_2) into the upper troposphere–lower stratosphere (UTLS). While ash typically settles out within weeks, SO_2 is oxidized into sulfate aerosols. These aerosols can persist in the stratosphere for months to years and be transported globally by atmospheric circulation, leading to significant climate impacts. Sulfate aerosols efficiently scatter incoming solar radiation back to space, producing a global net cooling in the lower troposphere (Minnis et al., 1993; Tabazadeh et al., 2002; Thompson and Solomon, 2009; Solomon et al., 2011). For instance, the 1991 eruption of Mount Pinatubo caused a global surface temperature decrease of approximately $0.5\,^{\circ}\mathrm{C}$ over the subsequent two years (McCormick et al., 1995). Reconstructions based on satellite observations for 1979–2015 indicate that clusters of moderate eruptions since 2004 have imposed a persistent negative radiative forcing of about $-0.08\ \mathrm{W\,m^{-2}}$ (Schmidt et al., 2018). For 2014–2022, stratospheric injections from volcanic eruptions and wildfires produced a global-mean effective radiative forcing of about $-0.18\ \mathrm{W\,m^{-2}}$ (Yu et al., 2023). In addition, enhanced aerosol surface-area density promotes heterogeneous chemistry on polar stratospheric clouds, thereby accelerating ozone depletion (Hofmann and Solomon, 1989; Portmann et al., 1996; Solomon, 1999; Zuev et al., 2015; Solomon et al., 2016).

Several key factors govern the climate impact of volcanic aerosols from an eruption: (1) eruption magnitude; (2) injection height and self-lofting; (3) eruption latitude; and (4) dynamical evolution. (1) ~~The Volcanic Explosivity Index (VEI) serves as a proxy for eruption intensity (Newhall and Self, 1982), and events with VEI $\geq$ 4 can inject vast quantities~~ Eruption magnitude can be characterized by the amount of SO_2 ~~, water vapor, and ash , causing marked climate perturbations~~ and ash released, which largely controls aerosol formation potential and radiative forcing. Notably, substantial perturbations of stratospheric water vapour and aerosol microphysics have also been reported for the 2022 Hunga Tonga eruption despite modest SO_2 injection (Carn et al., 2022; Zhu et al., 2022). (2) Eruption products injected directly into the stratosphere ~~— or~~ , as well as volcanic plumes in the upper troposphere that self-loft ~~via radiative heating~~ into the lower stratosphere ~~— can persist far longer~~ through radiative heating, can persist much longer than plumes confined to the troposphere (Toohey et al., 2025). (3) Aerosols from tropical eruptions are transported most efficiently via the Brewer–Dobson circulation (Brewer, 1949; Dobson, 1956; Butchart, 2014) , whereas mid-latitude eruption aerosols can still reach the tropics through Rossby-wave breaking or transport by the Asian Summer Monsoon Anticyclone (ASMA) (Konopka et al., 2009; Kloss et al., 2021; Wu et al., 2023). (4) UTLS jet streams, cyclones, anticyclones, and stratospheric circulation govern dispersion patterns and dilution rates. ~~Note: Submarine eruptions can have high VEI yet modest stratospheric SO_2; for example, Hunga (2022; VEI 5–6) injected only ~0.5 Tg SO_2, while strongly perturbing stratospheric H_2O and aerosol microphysics (Carn et al., 2022; Zhu et al., 2022).~~

~~Among the various transport mechanisms influencing volcanic aerosol fate~~In the Northern Hemisphere summer, the ASMA ~~plays a particularly important role during the boreal summer~~is the dominant circulation system in the UTLS. Deep convection injects pollutants into the UTLS, where the ASMA's strong anticyclonic circulation acts as a dynamical transport barrier, ~~trapping those air masses in its circulation. Simultaneously, the barrier is permeable, and the horizontal outflow of the ASMA can transport monsoon air masses to~~ confining these air masses over Asia during ascent into the stratosphere (e.g., Park et al., 2007; Randel et al., 2010; Fadnavis et al., 2014; Santee et al., 2017; Vogel et al., 2019). However, as the ASMA boundary is not a strict transport barrier, air masses can be exported from the monsoon circulation into the extratropical UTLS ~~(Vogel et al., 2016; Yu et al., 2017). This dual role makes the ASMA a key element in understanding aerosol dispersion in the Northern Hemisphere following volcanic eruptions~~(Vogel et al., 2016; Yu et al., 2017). This combination of confinement and export is important for interpreting aerosol dispersion during boreal summer, including the dispersion of volcanic aerosol. Previous work on the 2011 Nabro eruption debated whether its plume reached the stratosphere directly or was lofted by monsoon ascent. Bourassa et al. (2012) proposed that the plume remained in the upper troposphere and was subsequently transported into the stratosphere by large-scale ascent in the monsoon, whereas later studies showed evidence of direct stratospheric injection, independent of monsoon-driven lifting (e.g., Fromm et al., 2013; Vernier et al., 2013).

The mid-latitude Raikoke volcano ~~(48°N, 153°E)~~ erupted on 21–22 June ~~2019 (VEI 4), and its aerosol plume was advected through the ASMA during the anticyclone's mature phase, providing an ideal case to examine how the ASMA modulates volcanic plume transport.~~ 2019. Raikoke injected ~ 1.5 Tg of SO_2 into the lower stratosphere (Cai et al., 2022; Vernier et al., 2024). Subsequently, ash-driven radiative heating lofted parts of the volcanic plume, raising the volcanic cloud top above $20\,\mathrm{km}$ within four days (Muser et al., 2020; Gorkavyi et al., 2021). Three days after the eruption, compact anticyclonic "vorticized volcanic plumes" (VVPs) detached from the main volcanic cloud, trapping more than half of the SO_2 mass (Khaykin et al., 2022). The primary VVP then rose to ~ 27 km, spanning ~ 400 km in width but only ~ 1.5 km in depth. Meanwhile, the residual main plume was diluted at lower altitudes, resulting in two distinct Raikoke plumes (Khaykin et al., 2022). In August 2019, part of the aerosol plume was transported into and through the ASMA during the mature stage of the boreal-summer anticyclone, providing an ideal case to examine how the ASMA modulates volcanic plume transport.

Beginning in August 2019, frequent balloon-borne measurements were conducted over Lhasa~~(29.66°N, 91.14°E), when the site lay inside the ASMA~~ , at UTLS levels ~~. The resulting~~ located within the ASMA as indicated by the ERA5 150 hPa geopotential height field (Fig. 1a). The profiles captured two pronounced aerosol layers at distinct altitudes ~~, corresponding to~~ that are consistent with the trailing filament of the VVP and the diluted main plume. ~~Here, we use these observations together with high-resolution,~~ We combine these observations with ERA5-driven CLaMS backward trajectories and global three-dimensional SO_2-based tracer simulations to investigate the source region, transport pathways, and transit times from Raikoke to the Tibetan Plateau~~measurement site. We constrain the latitude–longitude~~ . Here, SO_2-based refers to passive tracers initialized using the horizontal extent of the ~~tracer injection region using satellite~~ Raikoke SO_2 ~~column retrievals from TROPOMI (~~cloud derived from the Tropospheric Monitoring Instrument (TROPOMI) aboard Sentinel-5P (Theys et al., 2024). We ~~also incorporate Portable Optical Particle Spectrometer (POPS) data~~ further use POPS profiles from Lhasa and Boulder ~~(USA). This study investigates how the ASMA modulates UTLS volcanic plume transportfollowing the~~ to evaluate the

simulated plume evolution over the Northern Hemisphere. In particular, Boulder serves as an independent site outside the ASMA region to evaluate plume transport. In situ UTLS observations of volcanic aerosol are rare, particularly for the 2019 Raikoke eruption. Here we combine balloon-borne COBALD and POPS profiles with high-resolution ERA5-driven CLaMS backward trajectories and global three-dimensional SO_2-based tracer simulations to identify transport of the Raikoke plume through the Northern Hemisphere and into the ASMA, with particular attention to transport pathways and time scales. Specifically, we address the following research questions: (1) What are the key transport pathways of the Raikoke plume in the vicinity of the ASMA? (2) Which processes dominate plume dilution? ~~Additionally~~In addition, we quantify the sensitivity of the ~~model simulations to different parameters and settings (e.g.,~~ simulations to key model settings (parameterized mixing intensity, injection height, and injection region).

The remainder of the paper is organized as follows: Section 2 describes data and methods; Section 3 presents balloon observations from Lhasa and Boulder; Section 4 reports ~~CLaMS transport results and sensitivity analyses~~the backward-trajectory analysis and global CLaMS transport simulations; Section 5 ~~estimates self-lofting heights~~discusses modelling sensitivities, including sensitivities to parameterized mixing, injection-region definition, and injection height; Section 6 concludes; and ~~Section 7~~ Appendix A presents supplementary material.

2 Data and Methods

2.1 ~~Balloon-borne~~ Balloon-borne Instruments

Volcanic aerosol profiles at Lhasa ~~(29.66°N, 91.14°E)~~ were obtained during the 2019 Asian Summer Monsoon (ASM) season as part of the Sounding Water Vapor, Ozone, and Particles (SWOP) campaign. The SWOP campaign was led by the Institute of Atmospheric Physics, Chinese Academy of Sciences. Balloons were equipped with an electrochemical concentration cell (ECC) ozonesonde, a cryogenic frostpoint hygrometer (CFH), a compact optical backscatter aerosol detector (COBALD), and an ~~iMet radiosonde . ECC~~ International Met Systems (InterMet) iMet-1-RSB radiosonde (GRUAN Lead Centre, 2025). However, ECC ozone measurements are not analyzed in this study. A total of nine measurements occurred in July–August (one in July, eight in August), followed by monthly measurements through January 2020. On 20 August 2019, the payload also included a Portable Optical Particle Spectrometer (POPS). During July–August 2019, Lhasa lay within the interior of the ASMA at UTLS levels (Fig. 1a). The site was chosen to observe the Raikoke plume ~~as it circulated within the anticyclone~~ in the ASMA interior and to document its arrival and vertical evolution. Additional information on SWOP field activities and on campaigns conducted in other years is available in Bian et al. (2012); Li et al. (2017, 2018, 2020); Ma et al. (2022); Yang et al. (2023).

The POPS data over Boulder were provided by the Baseline Balloon Stratospheric Aerosol Profiles (B^2SAP) project; we analyze five profiles—three influenced by the Raikoke eruption (two in August 2019 and one in November 2019) and two background references on 28 June 2019 and 3 December 2019 (Todt et al., 2023).

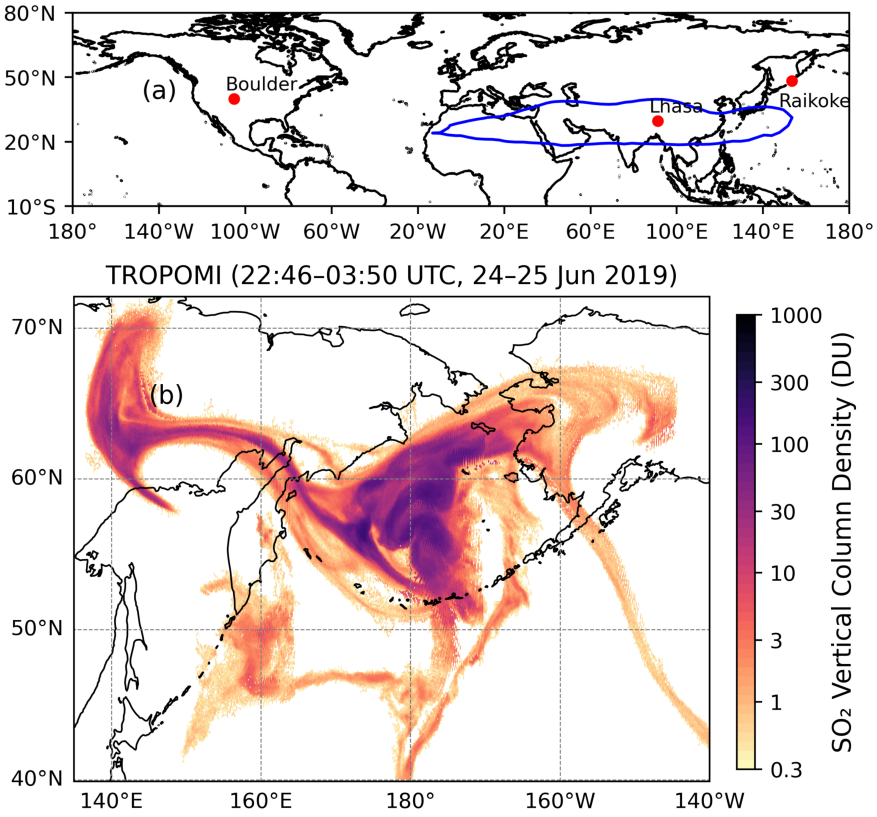

Figure 1. (a) ~~Red markers show~~ Map showing the ~~geographic~~ locations of the ~~Raikoke volcano,~~ balloon measurement sites over Lhasa (29.7°N, 91.1°E) and Boulder (39.9°N, 105.2°W), and the Raikoke volcano (48.3°N, 153.3°E). The blue contour shows the ERA5 geopotential height at 150 hPa averaged over August 2019 at 00 UTC. The 14.32 km contour is used here as an indicator of the ASMA at UTLS levels. (b) Spatial distribution of SO_2 vertical column density (DU) from TROPOMI, retrieved with an assumed plume height of 15 km, using orbits from 22:46 UTC on 24 June to 03:50 UTC on 25 June 2019.

Figure 1a shows the geographic locations of Raikoke volcano and the balloon-sounding sites at Lhasa and Boulder. An overview of the analyzed balloon flights at Lhasa and Boulder, including the identified plume-layer ranges, is provided in Table 1.

The Compact Optical Backscatter Aerosol Detector (COBALD) was developed by ETH Zurich (Brabec et al., 2012). Its lightweight and portable design makes it suitable for balloon payloads used in the study of cirrus clouds (Brabec et al., 2012; Cirisan et al., 2014; Reinares Martínez et al., 2021; Yang et al., 2023) and aerosols (Vernier et al., 2015; Brunamonti et al., 2018; Hanumanthu et al., 2020). COBALD uses two ~~high-power~~ high-power LEDs emitting at 455 nm (blue) and 940 nm (near-infrared). It measures backscattered light from air molecules and particles, including aerosols and cloud particles (e.g.

ice crystals). The backscatter ratio (BSR) is defined as

$$\mathrm{BSR} = \frac{\beta_{\mathrm{air}} + \beta_{\mathrm{particles}}}{\beta_{\mathrm{air}}} \frac{\beta_{\mathrm{air}} + \beta_{\mathrm{particles}}}{\beta_{\mathrm{air}}}, \tag{1}$$

where ~~β_{air}~~ β_{air} is the backscatter coefficient of air molecules and ~~$\beta_{\mathrm{particles}}$~~ $\beta_{\mathrm{particles}}$ is the backscatter coefficient of aerosols or cloud particles. The instrument measures only the total backscatter ($\beta_{\mathrm{total}} = \beta_{\mathrm{air}} + \beta_{\mathrm{particles}}$); β_{air} is calculated in post-processing from Rayleigh scattering using the measured pressure and temperature profiles, and $\beta_{\mathrm{particles}}$ is obtained as $\beta_{\mathrm{total}} - \beta_{\mathrm{air}}$. Here, BSR_{455} represents the backscatter ratio at 455 nm. The instrument's field of view is $\pm 6°$, and its detection range spans 0.5–10 m. Because sunlight severely interferes with the measurements, COBALD is only operated at night. ~~The maximum~~ COBALD BSR uncertainty is ~~1.3 % at 940 nm and 0.2 % at 455 nm at ground level. At 10 km altitude, uncertainties increase to~~ typically characterized by an absolute error interval of about ~5 % ~~and~~ for the profile, while the precision is better than ~1 % ~~at 940 nm and 455 nm, respectively (Vernier et al., 2015)~~under UTLS conditions (Vernier et al., 2015; Brunamonti et al., 2021; Reinares Mart

.

The COBALD color index (CI) is defined as

$$\mathrm{CI} = \frac{\mathrm{BSR}_{940} - 1}{\mathrm{BSR}_{455} - 1}, \tag{2}$$

which serves as an empirical proxy for particle size within aerosol layers. Note that when BSR_{455} and BSR_{940} are close to 1, CI can become sensitive to small baseline or calibration offsets.

The Cryogenic Frostpoint Hygrometer (CFH) is a high-precision instrument for measuring water vapor based on the chilled mirror principle. It controls the mirror temperature to maintain a stable frost- or dew-point. Combined with temperature and pressure data from the iMet radiosonde, the relative humidity over ice (~~$\mathrm{RH}_{\mathrm{ice}}$~~ $\mathrm{RH}_{\mathrm{ice}}$) is calculated using the empirical equation from Murphy and Koop (2005):

$$\mathrm{RH}_{\mathrm{ice}} = \frac{e_{\mathrm{ice}}(T_{\mathrm{mirror}})}{e_{\mathrm{ice}}(T_{\mathrm{environment}})} \frac{\mathrm{e_{ice}(T_{mirror})}}{\mathrm{e_{ice}(T_{environment})}}, \tag{3}$$

where ~~T_{mirror}~~ $\mathrm{e_{ice}(T)}$ is the saturation vapour pressure over ice at temperature T (in Kelvin), $\mathrm{T_{mirror}}$ is the measured ~~frost-point temperatureand~~ ~~$T_{\mathrm{environment}}$~~ frost-point temperature, and $\mathrm{T_{environment}}$ is the ambient air temperature. ~~The measurement uncertainty is approximately~~ CFH uncertainties may be as low as ~2 % in the lower troposphere and ~~increases to~~ ~5 % near the tropical tropopause ~~(Vömel et al., 2016).~~ under good operating conditions (Vömel et al., 2016). For UTLS conditions we use a conservative uncertainty of ±10 % (Fahey et al., 2014; Poltera et al., 2025).

The Portable Optical Particle Spectrometer (POPS) is a lightweight instrument for measuring aerosol number density and size distribution (Gao et al., 2016). POPS employs a 405 nm laser to detect light scattered by individual particles, with scattering intensity related to particle size. It measures particles from 140 nm to 2,500 nm and reports number concentrations in size bins (Todt et al., 2023). Measurement uncertainties are dominated by particle sizing (including sensitivity to the assumed refractive index) and flow-rate calibration ~~(Gao et al., 2016; Mei et al., 2020)~~(Gao et al., 2016).

2.2 TROPOMI

TROPOMI, the satellite instrument aboard ESA's sun-synchronous Sentinel-5P platform launched ~~on 13 October~~ in 2017, is a hyperspectral imaging spectrometer that records back-scattered radiation from the ultraviolet to the shortwave infrared (Veefkind et al., 2012). Total-column SO_2 in Dobson units ($1\,\mathrm{DU} = 2.69 \times 10^{16}\,\mathrm{molec/cm^2}$) is retrieved using differential optical absorption spectroscopy (DOAS) applied to three wavelength windows (312–326 nm, 325–335 nm, 360–390 nm) (Theys et al., 2017, 2024). The publicly available Level 2 product provides four vertical columns: the surface–to–top-of-atmosphere column and three columns assuming an SO_2 plume centered at 1, 7, or 15 km altitude. Following previous Raikoke studies (Muser et al., 2020; de Leeuw et al., 2021; Cai et al., 2022), we adopt the 15 km retrieval, which most closely matches the eruption's mean injection height; values below the instrument's 0.3 DU detection limit are excluded~~(Theys et al., 2024)~~, following Theys et al. (2024). Four consecutive TROPOMI overpasses of the SO_2 vertical column density at 15 km altitude captured the entire Raikoke SO_2 cloud between 22:46 UTC on 24 June and 03:50 UTC on 25 June 2019 (Fig. 1b).

2.3 CLaMS

The Chemical Lagrangian Model of the Stratosphere (CLaMS) is a chemistry–transport model that calculates the three-dimensional motion of air parcels, which in turn represent the model grid (McKenna et al., 2002; Pommrich et al., 2014). ~~CLaMS is applied here to investigate the transport of the volcanic plume following the Raikoke eruption. In the vertical direction it employs an isentropic coordinate aligning layers with constant potential temperature θ, making the model well suited for stratospheric processes. The CLaMS vertical coordinate — the hybrid coordinate~~ The CLaMS hybrid vertical coordinate (ζ ~~— follows~~) follows orography near the surface and transitions smoothly into θ once $\sigma = p/p_{\mathrm{surf}}$ reaches 0.3 (usually about 300 hPa) (Pommrich et al., 2014). The isentropic coordinate in CLaMS is well suited for representing transport and mixing in the stratosphere. All CLaMS applications in this study—both backward trajectories and three-dimensional simulations with SO_2-based tracers—are driven by ERA5 reanalysis: the ~~main~~ standard runs use the native hourly fields on the $0.3^\circ \times 0.3^\circ$ (latitude $\times$ longitude) grid with 137 vertical levels up to 80 km (Hersbach et al., 2020), whereas the sensitivity experiment in Appendix Figure A2 repeats the simulation with ERA5 ~~data down-sampled to~~ fields at $1^\circ \times 1^\circ$ ~~and every 6 h. Compared to ERA-Interim, ERA5 improved the Lagrangian transport representation in the troposphere and cross-tropopause exchange (Hoffmann et al., 2019; Li et al., 2020), as well as within the Asian monsoon region (Clemens et al., 2024; Vogel et al., 2024)~~ spatial and 6 hours temporal resolution.

Diabatic backward trajectories are initialized every second along the balloon's vertical ascent profile, using the in-situ measurements of temperature (for deriving potential temperature), pressure, time, longitude, and latitude to define the start positions. Vertical velocities were computed from ERA5 wind fields and total diabatic heating rates, including clear-sky and cloud radiation, latent heat release, and turbulent and diffusive transport (Ploeger et al., 2021). This approach captures uplifts by resolved convection as represented in ERA5 (Li et al., 2020; Clemens et al., 2024; Vogel et al., 2024). To identify the volcanic influence, only those backward trajectories that passed through the Raikoke eruption region (Fig. 1b) during 22:46 UTC on 24 June and 03:50 UTC on 25 June 2019 were retained.

~~The global~~ Global three-dimensional ~~CLaMS transport simulations include the CLaMS-specific parameterization of small-scale, unresolved mixing processes induced by shear-driven stirring in the large-scale flow (Konopka et al., 2004). Based on the TROPOMI 15 km~~ transport simulations use passive SO_2-based tracers initialized from the horizontal extent of the Raikoke SO_2 ~~product shown in~~ cloud in the TROPOMI 15-km product (Fig. 1b~~, we used the Raikoke plume's overall latitude–longitude extent (~~; four overpasses between 22:46 UTC on 24 June and 03:50 UTC on 25 June 2019; values ~~≥ 0.3~~~~≥ 0.3 DU) ~~as the tracer injection mask; only the spatial extent, not the column amplitude, was used~~(Theys et al., 2024). At 00:00 UTC on 25 June 2019, parcels inside this mask ~~within prescribed potential-temperature ranges (380–400, 400–420, 420–440 K) were~~ are initialized to 1 ~~inside the mask~~ (0 outside) ~~for the SO_2-based tracer~~ within three potential-temperature ranges (380–400 K, 400–420 K, and 420–440 K) and then advected and mixed globally, ~~such that mixing yields fractional values~~ yielding tracer fractions between 0 and 1.

To assess how different mixing intensities influence the reconstruction of volcanic plume transport processes, two simulations were conducted: (i) a control simulation with mixing every ~~24 h and a critical Lyapunov exponent (λ_c) of 1.5~~24 hours and $\lambda_c = 1.5$ (a commonly used set-up for CLaMS simulations driven by high-resolution ERA5 reanalysis data; Vogel et al. (2025)); (ii) a modified simulation with mixing every ~~6 h~~ 6 hours and $\lambda_c = 3.5$. ~~Primarily, we focus on~~ In the CLaMS mixing scheme, parameterized mixing is triggered when the integral deformation between neighboring air parcels exceeds an empirical critical deformation $\gamma_c = \lambda_c \Delta t$, where λ_c is the critical Lyapunov exponent and Δt is the advective time step (mixing interval). For a given Δt, a larger λ_c (thus a larger γ_c) requires stronger deformation to trigger mixing and therefore corresponds to less frequent parameterized mixing (and vice versa) (Konopka et al., 2004, 2007). In our setup, the modified simulation ~~results, since they provide better agreement with~~ corresponds to enhanced parameterized mixing compared to the control simulation. Throughout most of the paper we show results from the modified simulation, as these agree better with the observations. Sensitivity to parameterized mixing intensity ~~is~~ and comparisons with the control simulation are discussed in Sect. ~~4.3 (modelling sensitivities) . Together with the backward-trajectory analysis, these simulations provide a comprehensive view of the plume's large-scale dispersion.~~ 5.1. The mixing configurations and the additional sensitivity runs (rectangular mask and coarser ERA5 input) are summarized in Table 2.

Table 1. Summary of analyzed balloon flights at Lhasa and Boulder, including sequential flight ID, date, mid-ascent time (UTC), key instruments used in this study, and the potential temperature (θ) and pressure (p) ranges of the observed volcanic plume layer. The plume layer was identified from COBALD measurements where $BSR_{455} > 1.1$ and $CI > 6$, and from POPS measurements where the particle number concentration exceeded 150 cm^{-3}. Mid-ascent time denotes the midpoint of the ascent period from launch to balloon burst. The "Key instruments" column lists only the instruments analyzed in this work; additional payload components were flown but are not listed here. A dash (–) denotes that no volcanic plume layer was identified for that flight.

Site	Flight ID	Date	Mid-ascent time (UTC)	Key instruments	Observed plume layer: θ (K)	Observed plume layer: p (hPa)
Lhasa	F01	30.07.19	17:58	COBALD CFH	–	–
	F02	01.08.19	15:45	COBALD CFH	–	–
	F03	03.08.19	15:23	COBALD CFH	410–422; 459–472	78–71; 59–56
	F04	06.08.19	15:26	COBALD CFH	404–416	82–75
	F05	08.08.19	15:10	COBALD CFH	389–423	98–73
	F06	10.08.19	16:05	COBALD CFH	397–422	84–70
	F07	12.08.19	15:49	COBALD CFH	398–426	84–71
	F08	15.08.19	17:24	COBALD CFH	406–423	79–71
	F09	20.08.19	17:14	COBALD CFH POPS	393–434	89–68
	F10	30.09.19	15:34	COBALD CFH	385–452	96–64
	F11	28.10.19	15:24	COBALD CFH	390–459	100–60
	F12	24.11.19	15:09	COBALD CFH	410–482	79–55
	F13	04.01.20	15:29	COBALD CFH	393–399; 415–432	118–115; 99–91
Boulder	F14	28.06.19	17:05	POPS	–	–
	F15	07.08.19	17:08	POPS	373–442	122–73
	F16	27.08.19	16:38	POPS	385–429; 480–505	117–80; 59–52
	F17	08.11.19	17:58	POPS	389–435	107–76

Table 2. Summary of tracer simulations using different injection-region definitions (satellite SO_2 plume mask and a rectangular domain), including injection layer, mixing interval, and critical Lyapunov exponent (λ_c).

Simulation	Injection region	Injection layer	Mixing interval	λ_c	Notes
All simulations listed below are driven by ERA5 at $0.3^\circ \times 0.3^\circ$ *spatial and 1 hour temporal resolution. Figure A2 shows the* SO_2*-based_Control simulation repeated with coarser ERA5 input (*$1^\circ \times 1^\circ$ *spatial, 6 hours temporal resolution).*					
SO_2-based_Control	satellite SO_2 plume mask	380–400 K; 400–420 K; 420–440 K	24 hours	1.5	reference run
SO_2-based_Modified	satellite SO_2 plume mask	380–400 K; 400–420 K; 420–440 K	6 hours	3.5	main run; best agreement with observations
rectangle-based_Modified	(163°E–170°W, 49°N–62°N)	380–400 K; 400–420 K; 420–440 K	6 hours	3.5	sensitivity to injection-region definition

3 Measurement Results

The COBALD–CFH tandem provides a practical method for identifying cirrus clouds and aerosol layers because collocated backscatter and frost-point humidity measurements allow a straightforward separation of ice-cloud signatures from aerosol enhancements (Brabec et al., 2012; Cirisan et al., 2014; Reinares Martínez et al., 2021; Yang et al., 2023). Cirrus clouds are identified using the criteria $\mathrm{BSR}_{455} > 1.2$~~and $\mathrm{RH}_{\mathrm{ice}} > 70\%$~~, $\mathrm{RH}_{\mathrm{ice}} > 70\%$ and $\mathrm{CI} > 7$ (Vernier et al., 2015; Brunamonti et al., 2018; Hanumanthu et al., 2020; Yang et al., 2023). These clouds are shown as gray-shaded regions in Fig. 2. On 30 July 2019, ~~$\mathrm{RH}_{\mathrm{ice}}$~~ $\mathrm{RH}_{\mathrm{ice}}$ reached $\sim 90\%$ at 423 K (70 hPa), but no corresponding enhancement in BSR_{455} was observed; thus, this layer is not classified as cirrus by our joint criterion and likely represents a moist, ice-free layer. When cirrus ~~clouds and aerosols coexist, it becomes difficult to isolate the aerosol signal~~ and aerosols occur within the same profile, aerosol and cloud signals can generally be separated if they are vertically distinct (e.g., using BSR and CI), whereas if a cirrus cloud overlaps the aerosol layer at the same altitude, the aerosol contribution cannot be reliably isolated because cirrus BSR_{455} ~~values are significantly higher than those of aerosols. Regions showing enhanced BSR_{455}—most likely due to Raikoke aerosols—are empirically~~ typically dominates. Thus, the aerosol cannot be reliably detected or quantified under such conditions. Using these criteria, we exclude cirrus-contaminated layers. Remaining enhancements with $\mathrm{BSR}_{455} > 1.1$ are treated as aerosol layers and then classified using a CI threshold of 6: layers attributed to the Raikoke plume ($\mathrm{CI} > 6$) are highlighted in orange in Fig. ~~2. On~~ 2, while layers more consistent with ATAL aerosol ($\mathrm{CI} < 6$) are highlighted in light blue. We note that CI is used here as an additional indicator within aerosol layers and should be interpreted with caution, and that the ATAL identification in our dataset is limited. In very clean air where BSR values at both wavelengths approach 1, CI can become unstable; we therefore apply CI only within aerosol layers with $\mathrm{BSR}_{455} > 1.1$ after excluding cirrus. On 3 August 2019, ~~40~~ 42 days after the Raikoke eruption, ~~a potential enhancement appeared at 479–492 K (54–51 hPa). On 3 August,~~ two distinct BSR_{455} peaks were observed: the upper peak at 459–472 K (59–56 hPa) reached the maximum value recorded in Lhasa (~ 1.8), and the lower peak at ~~410–429 K (77–70 hPa~~410–422 K (78–71 hPa) had a somewhat weaker magnitude (~ 1.4). On 6 August 2019, another sharp peak appeared at ~~404–418 K (82–74 hPa~~404–416 K (82–75 hPa). After 8 August 2019, the peaks became less sharp and more vertically extended, which persisted until 24 November 2019. By 4 January 2020, ~~no volcanic aerosol signal was evident~~the aerosol backscatter enhancement had further weakened, and no distinct peak was observed in the profile.

~~The median BSR~~In general, ATAL-related enhancements in COBALD BSR_{455} ~~values in 2019, associated with the Raikoke aerosol, peaked at ~ 1.24—higher than the ATAL peak in 2013 (~ 1.10; Fig. 3a). Typical ATAL~~ profiles are largely confined to ~~360–400 K~~ 360–400 K (core near ~~370–390 K~~370–390 K), with occasional extensions up to ~~420–440 K~~ 420–440 K depending on region and year (Vernier et al., 2015, 2018; Appel et al., 2022). The ATAL profile from 2013 shown in Fig. 3a is taken from the COBALD measurements over Lhasa reported by Vernier et al. (2015). The 2019 median peak occurs near ~~417 K, about 33 K above the~~ 417 K, about 33 K above the 2013 ATAL peak (~~384 K), highlighting a vertical signature that differs markedly from a typical ATAL profile~~384 K), corresponding to roughly 1.7 km in altitude in the UTLS (based on the 30 July 2019 background sounding). The vertical extent of ATAL enhancements varies across regions and years; therefore, we emphasize

the peak magnitude as the more robust difference: the 2019 Raikoke-related median BSR_{455} reaches ∼1.25, exceeding the 2013 ATAL peak (∼1.10; Fig. 3a).

All POPS particle number densities are converted to standard temperature and pressure (STP; 1013 hPa, 273.15 K) to remove the pressure-driven decline with altitude (Fig. 3b). At Boulder, no clear volcanic aerosol signal was present on 28 June 2019, and by 3 December 2019 the profile shows no obvious volcanic aerosol peak (Fig. 3b). The particle number density at Lhasa on 20 August 2019 was lower than that at Boulder on 7 August and 27 August 2019. This is consistent with the global CLaMS tracer simulations (Sect. 4.2; cf. Figs. 7 and 8), which show that the main Raikoke plume is transported along the subtropical westerly jet in the mid-latitude UTLS, while transport into the ASMA interior is more limited due to the anticyclone acting as a partial horizontal barrier. Section 4 presents backward-trajectory calculations and ~~SO_2-based~~ three-dimensional tracer simulations with CLaMS to verify the origin and transport pathways of the ~~volcanic plume reaching Lhasa within the ASMA~~plume observed over Lhasa and Boulder.

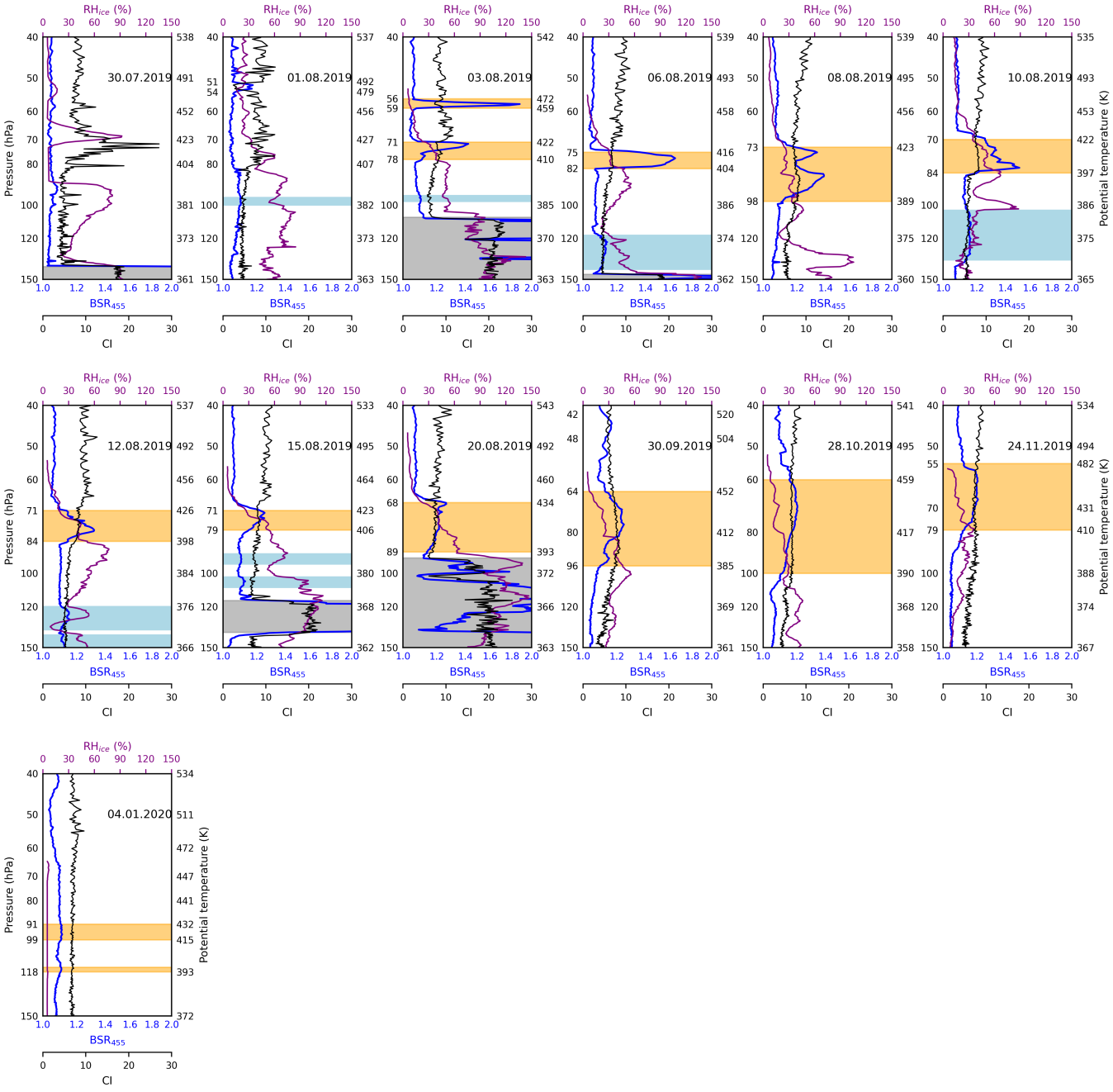

Figure 2. COBALD ~~(blue lines)~~ and CFH ~~(purple lines) measurements in~~ profiles above Lhasa from 30 ~~-~~July ~~-~~2019 to 4 ~~-~~January ~~-~~2020. ~~Dashed~~ COBALD backscatter ratio at 455 nm (BSR_{455}, blue) and COBALD color index (CI, black~~lines: -~~) are shown together with CFH relative humidity over ice (RH_{ice}, magenta). Pressure is given on the left axis and the corresponding potential temperature ~~°C~~on the right axis. Orange shading ~~:~~ marks the Raikoke ~~eruption impact~~influenced aerosol layers used to initialize the backward trajectories. Light blue shading indicates lower altitude aerosol enhancements attributed to ATAL that are not used for the plume initialization. Gray shading ~~:~~ ~~presence of~~ indicates cirrus ~~clouds~~conditions.

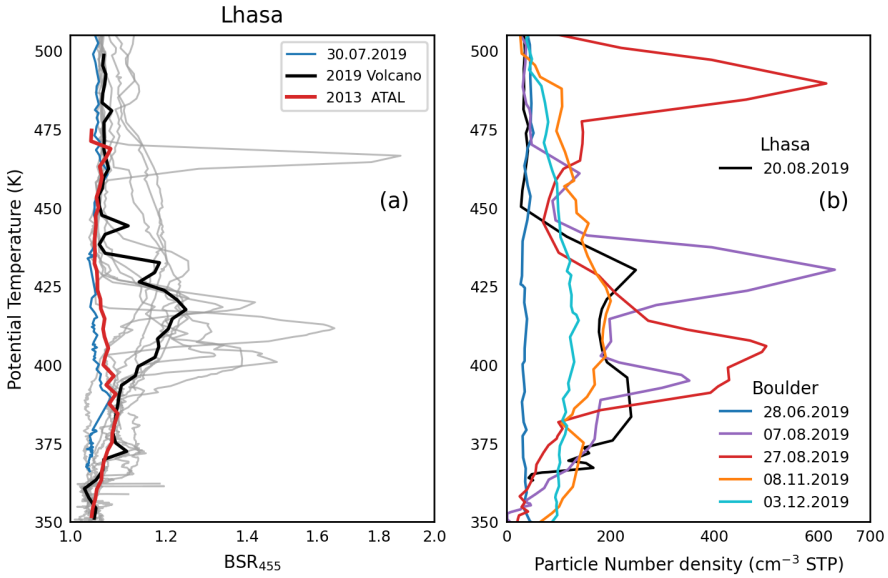

Figure 3. (a) COBALD measurements in Lhasa. The black line represents the median BSR_{455} ~~affected~~ for the 2019 profiles influenced by the volcanic ~~eruption in 2019.~~ event, and the gray lines show the corresponding individual profiles. The red line shows the median BSR_{455} during the ATAL in 2013. The blue line corresponds to the BSR_{455} on 30 July 2019, which was not affected by the Raikoke eruption. ~~The thin gray lines indicate individual profiles influenced by the volcanic event.~~ (b) POPS measurements in Boulder and Lhasa.

4 Results of CLaMS transport simulations

4.1 Backward-Trajectory Calculations

To verify that the enhanced aerosol ~~layer~~ layers observed over Lhasa ~~originated from~~ are linked to the Raikoke eruption, we ~~performed backward -trajectory analyses based on in-situ balloon-borne measurements over Lhasa, driven by high-resolution ERA5 data~~ calculated ERA5-driven diabatic backward trajectories with CLaMS (Fig. 4). ~~Backward trajectories were launched~~ Trajectories were released every second along ~~the balloon 's vertical ascent in the potential temperature range where an enhanced BSR_{455} was observed~~ each balloon ascent within the selected plume-layer potential-temperature intervals (orange shading in Fig. 2~~, and traced back to the eruption period. The start positions of the~~), using the iMet-derived time and location (longitude, latitude, pressure, and temperature) as initial conditions. All trajectories were calculated ~~using iMet radiosonde measurements.~~

~~The enhanced BSR_{455} was first detected over Lhasa on 1 August~~backward to a single common reference time (21 June 2019, ~~40 days after the Raikoke eruption, with pronounced peaks observed~~ 18:00 UTC), which serves as the trajectory endpoint for all cases.

Pronounced BSR_{455} peaks were observed over Lhasa on 3 August and 6 August 2019 (Fig. 2). ~~On 1 August and for~~ For the upper layer on 3 August 2019, backward trajectories indicate that the air parcels were transported approximately along isentropic surfaces (Fig. 4). By contrast, the lower layer on 3 August 2019 includes trajectories lofted from $\sim 370\,\mathrm{K}$ to $\sim 410\,\mathrm{K}$. In the ~~layer on 1 August and in the~~ upper layer on 3 August 2019, the transport pathways differed significantly from other layers, as evidenced by changes in longitude (see Fig. 5 for trajectory details). This suggests that the enhanced BSR_{455} resulted from volcanic aerosols originating from two distinct branches of the volcanic plume at different altitudes, each following a different transport pathway. From 8–20 August 2019, mixing from lower potential-temperature levels began to occur. This coincided with a decrease in BSR_{455} values in the in-situ measurements, as air with relatively low aerosol concentrations dilutes the enhanced signals. Over the following three months, as the ASMA weakened seasonally, air from lower potential-temperature levels increasingly influenced the Lhasa profiles. During this period, ~~volcanic signatures in the profiles no longer exhibited extreme~~ peak BSR_{455} ~~values, indicating that the enhanced~~ within the identified plume layer (orange shading in Fig. 2) decreased from values up to 1.88 in early August 2019 (95th percentile up to 1.77) to $\leq$1.25 from 30 September to 24 November 2019 (95th percentile $\leq$1.24), indicating progressive dilution of the volcanic aerosol layer ~~was mixed with~~ by relatively aerosol-poor air from the lower troposphere.

To illustrate air masses influenced by the Raikoke eruption, we filtered backward trajectories to include only those passing through the eruption region (Fig. 1b) between 22:46 UTC on 24 June 2019 and 03:50 UTC on 25 June 2019. We then examined several representative pathways to show how the volcanic plume entered the ASMA interior (Fig. 5). In Fig. 5, the reported fraction is ~~the percentage of the total backward trajectories~~ defined as (number of trajectories that meet the eruption-region criterion) / (total number of backward trajectories initialized for the corresponding flight date and θ layer shown in Fig. 4~~that pass through the eruption-region mask during that window~~). For the six cases shown in Fig. 5, the total numbers of initialized trajectories are 79 and 50 (03 August 2019, two θ layers), 72 (06 August 2019), 190 (08 August 2019),

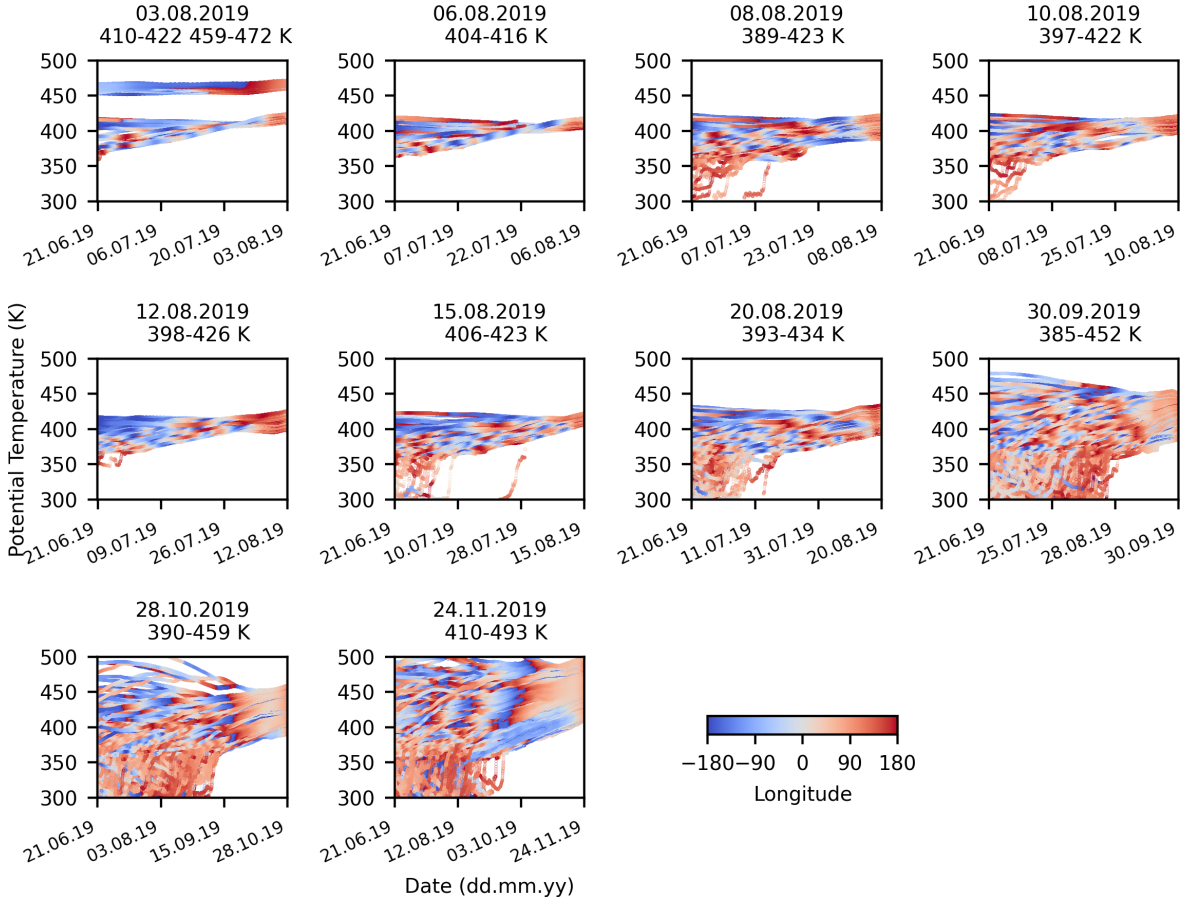

Figure 4. Backward trajectories initialized from the Lhasa balloon observations and traced back to the Raikoke eruption reference time (~~21–22~~ 21 June ~~–~~2019, 18:00 UTC). Only trajectories initialized within the enhanced BSR_{455} ~~potential-temperature~~ potential-temperature range (orange shading in Fig. ~~–~~2) are shown. Colors indicate trajectory longitude. The x-axis shows date (dd.mm.yy) along the backward integration (right: balloon initialization time; left: eruption reference time).

165 (10 August 2019), and 105 (12 August 2019). Because this filtering criterion is highly selective, only a small fraction of trajectories ~~remain~~remains, and the resulting fractions can be regarded as conservative estimates. A sensitivity test shows that the fraction of backward trajectories reaching the eruption region is ∼3–10 % when using the original TROPOMI SO_2 footprint and satellite-pass time window, but increases to ∼12–28 % when applying a broader rectangular domain (137–215° E, 42–73° N) and extending the time window to 7 days. The retained trajectories still follow the same main transport pathways shown here, providing confidence in the identified transport patterns.

For the calculation on 3 August 2019, the trajectories are divided into two distinct branches. ~~One branch originates from 410–429 K and corresponds~~ The trajectories in the lower branch originate from 410–422 K and correspond to the main vol-

canic aerosol plume carried by the subtropical westerly jet. The ~~other~~ upper branch originates from 459–472 K. Satellite ~~tracking shows that the primary VVP was entrained in~~ observations from TROPOMI on Sentinel-5P indicate that the VVP core was entrained into the summertime easterlies around ~~20–25 July, circled the globe three times, and passed south of the Tibetan Plateau on 31 July . This pathway aligns with the backward trajectories~~ 20–25 July (Gorkavyi et al., 2021; Khaykin et al., 2022) . The backward trajectories initialized in the 3 August 2019 plume layer (459–472 K) in Fig. ~~5. Furthermore, the potential temperature measured by the satellite during its ASMA transit also closely matched~~ 5 are consistent with the late-July phase of this satellite-tracked pathway. The potential temperature of the VVP during its transit through the ASMA inferred from satellite detections also closely matches the altitudes of enhanced BSR_{455} ~~(Gorkavyi et al., 2021; Khaykin et al., 2022)~~(Gorkavyi et al., 2021; Khay . Meanwhile, lidar measurements in Wuhan (central China) on 30 July reveal that the VVP's core backscatter coefficient is ~~far~~ much greater than that of the main aerosol plume (Jing et al., 2023; He et al., 2024), implying that our measurements in this branch captured only the trailing filament of the VVP. Although both sets of air parcels ~~correspond~~ belong to the same ~~balloon-borne observation~~ balloon profile, they ~~represent entirely different transport pathways—originating from two distinct regions of the Raikoke plume at different altitudes and driven by different processes~~trace back to two distinct plume components: the lower-θ main plume in the subtropical westerly jet (~410–422 K) and the higher-θ VVP filament in the summertime easterlies (~459–472 K). This indicates different source altitudes within the Raikoke plume and distinct dynamical transport pathways.

From 6 to 20~~August~~ August 2019, the overall transport pattern remained similar to that on 6 ~~August—corresponding~~ August 2019—corresponding to the main volcanic aerosol plume primarily driven by the subtropical westerly jet. ~~However, after~~ After entering the ASMA, some air parcels ~~took different paths: they were advected clockwise within the ASMA's anticyclonic circulation. This clockwise advection diluted the aerosol concentration, contributing~~ deviate from the jet pathway and circulate within the anticyclonic region. This increased spreading of trajectories suggests dispersion and lateral mixing with surrounding air, which may contribute to the observed decrease in BSR_{455}.

Backward trajectories for the Boulder flights on 7 and 27 August 2019 are shown in Fig. 6. On 7 August 2019, an enhanced aerosol layer is observed between 373 and 442 K (particle number concentration $> 150\ \mathrm{cm}^{-3}$). The corresponding backward trajectories indicate transport to Boulder primarily along the subtropical westerly jet. On 27 August 2019, two volcanic layers are present. The upper layer (480–505 K) is associated with the VVP filament transported in summertime easterlies. The lower layer occurs at 385–429 K. To better illustrate the transport pathway, we plot only trajectories initialized between 405 and 410 K. These trajectories indicate that the plume had already traveled once around the globe before reaching Boulder.

4.2 Global three-dimensional CLaMS simulations with SO_2-based tracers

In global three-dimensional CLaMS simulations, ~~SO~~we use passive tracers initialized from the observed SO_2 ~~-based tracers were released within the defined region~~ plume mask (Fig. 1b)~~at potential-temperature levels of 400–420 K at~~ . We refer to these as SO_2-based tracers. At 00:00 UTC on 25 June 2019~~to simulate the dispersal of the volcanic plume. The sensitivity to injection height is discussed in Section 5 (estimation of self-lofting heights~~, the tracer is set to 1 inside the mask (0 outside) within three potential-temperature ranges (380–400 K, 400–420 K, and 420–440 K) and then advected and mixed throughout

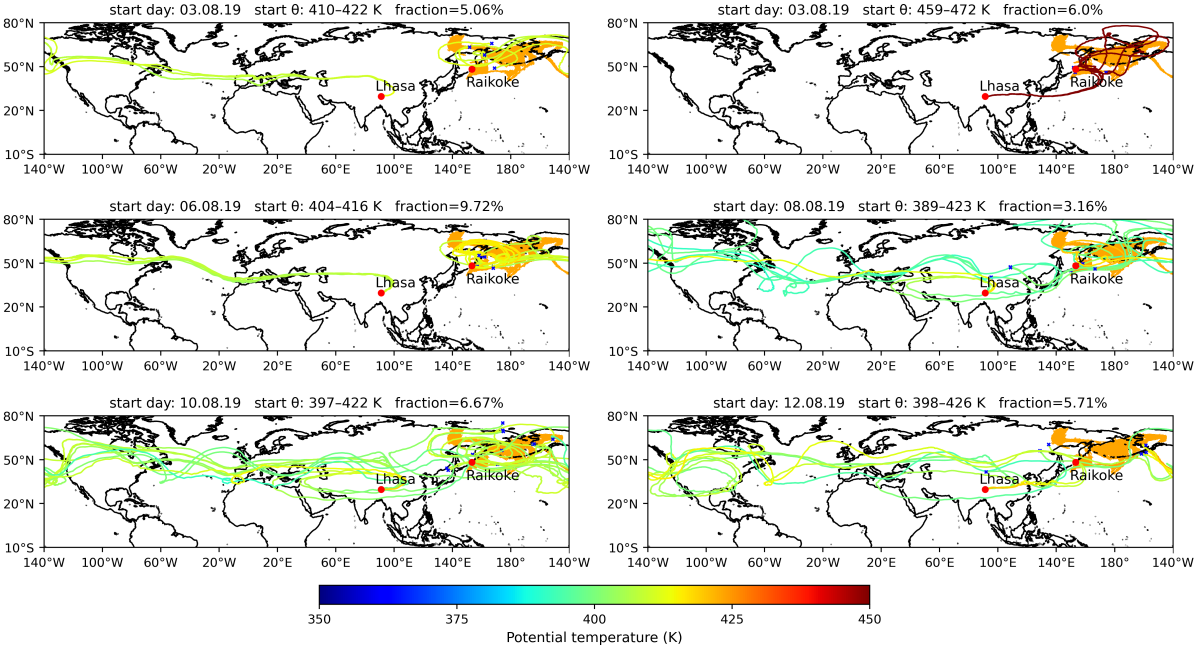

Figure 5. ~~Map showing representative backward~~ Backward trajectories ~~originating in~~ for the ~~volcanic eruption region~~Lhasa flights (3, ~~illustrating the main transport pathways from the eruption site to~~ 6, 8, 10, and 12 August 2019). Only trajectories that intersect the ~~Tibetan Plateau~~TROPOMI SO_2 mask between 24 June 2019, ~~with each trajectory shaded according to~~ 22:46 UTC and 25 June 2019, 03:50 UTC are shown. Trajectories are colored by potential temperature, and the SO_2 mask is shaded in orange. Panel titles give the start day, start θ range, and the fraction of trajectories that satisfy the SO_2 mask criterion. Locations of Lhasa and Raikoke are marked.

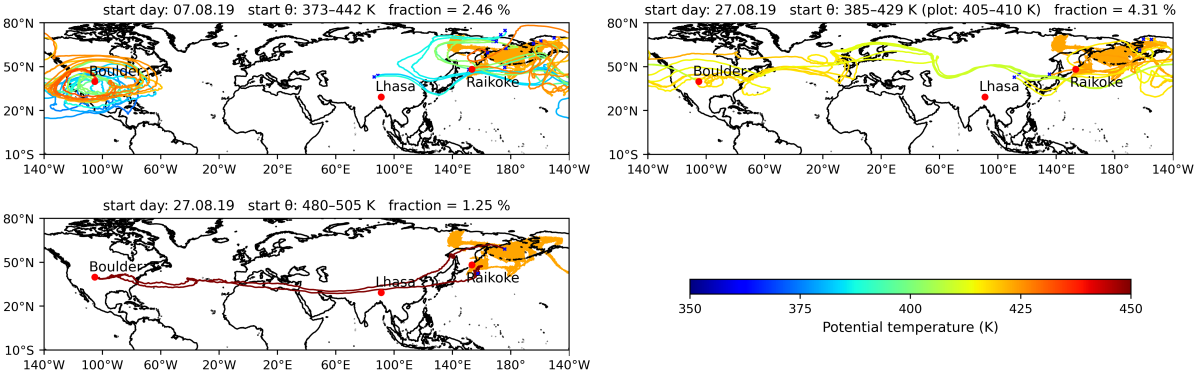

Figure 6. Same as Fig. 5, but for the Boulder flights (7 and 27 August 2019). For 27 August 2019, the fraction is computed for 385–429 K, while the plotted trajectories are restricted to 405–410 K to better illustrate the transport pathways. Locations of Boulder, Lhasa, and Raikoke are marked.

the global atmosphere in CLaMS. We present results for the 400–420 K release, while the 380–400 K and 420–440 K releases are used as sensitivity tests (Sect. 5.2; Figs. 11–12). Figure ~~6~~ 7 shows global maps ~~with~~ of fractions of the SO_2-based ~~tracers~~ tracer falling within the 400–420 K layer for each measurement day from 30 July to 20 August 2019, using the modified simulation~~(mixing every 6 h)~~. Here, the ~~fraction denotes the proportion of initialized tracer parcels that remain within the specified potential-temperature layer~~ tracer fraction (0–1) represents the fractional contribution of air originating from the volcanic plume (identified by the TROPOMI SO_2 mask shown in Fig. 1b) after advection and mixing. ~~At initialization, the tracer is set to 1 inside the eruption-region mask and 0 elsewhere; subsequent mixing yields values between 0 and 1.~~

The ASMA is indicated by the Montgomery streamfunction (Santee et al., 2017) at the $378 \times 10^3\,\mathrm{m^2\,s^{-2}}$ contour (layer mean over 400–420 K) as an estimate of its edge. The 11 PVU potential vorticity contour (layer mean over 400–420 K) ~~indicates the dynamical situation, showing in addition outflow of the ASMA~~ illustrates the isentropic transport, including ASMA outflow (filaments) and in-mixing of PV-rich air from high latitudes. The strong transport barrier of the ASMA observed within ∼ 370–390 K is much weaker above 400 K (Ploeger et al., 2015). The results shown in Fig. ~~6~~ 7 illustrate the overall intrusion of air masses into the ASMA and agree well with the Lhasa COBALD BSR_{455} observations. From 30 July to 1 August 2019, part of the SO_2-based ~~tracers~~ tracer entered the ASMA from its eastern side without reaching Lhasa. This is consistent with the absence of clear aerosol signals in the lower layers of the balloon-borne measurement data. On 3 August 2019 and 6 August~~,~~ ~~tracers~~ 2019, air masses impacted by the SO_2-based tracer arrived above Lhasa. Without a significant effect of upwelling from below at that time, the SO_2-based tracer signals remained sharp and concentrated. From 8 to 20 August, most of the ASMA contained mixed air masses. However, SO_2-based tracer fractions inside the ASMA remained lower than outside, reflecting the anticyclonic transport barrier. During August, only a minor fraction of the SO_2-based tracer is located inside the ASMA, while the majority remains outside. By later months, progressive mixing reduces the contrast between ASMA and surrounding regions in the tracer distribution (not shown here).

The corresponding SO_2-based tracer fractions within the 400–420 K layer over the North American continent are shown in Fig. 8. Elevated tracer fractions are simulated over Boulder on both 7 and 27 August 2019. By 8 November 2019, the overall tracer fractions are markedly lower, reflecting progressive dilution by mixing during transport.

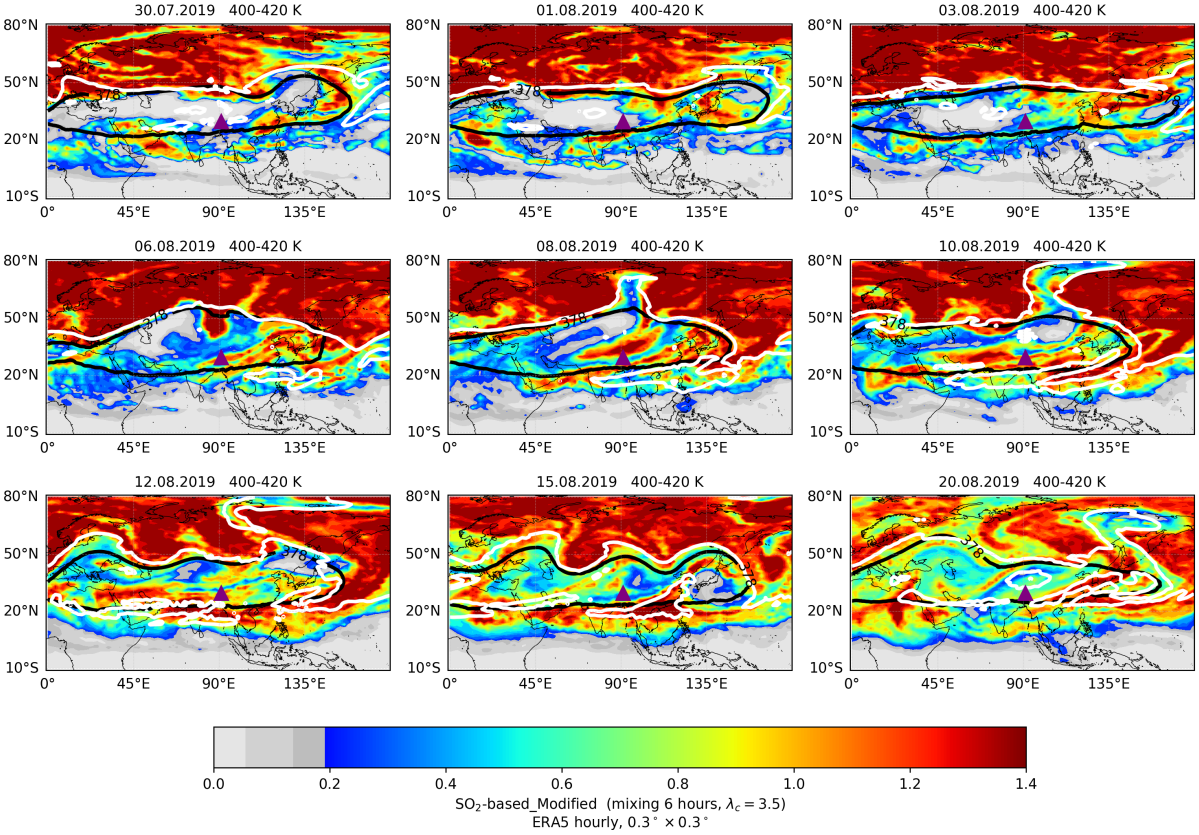

Figure 7. ~~Fractions of~~ SO_2-based ~~tracers~~ tracer fractions within the 400–420 K layer from the modified simulation (simulation details in Table 2). The purple triangle indicates Lhasa. The ASMA edge is shown by the black contour at the $378 \times 10^3\,\mathrm{m^2\,s^{-2}}$ Montgomery streamfunction. The white contour marks the 11 PVU potential vorticity ~~boundary~~isoline.

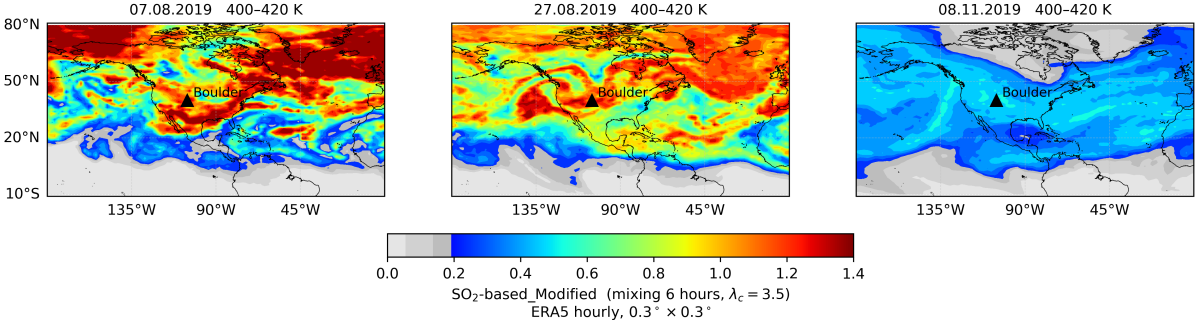

Figure 8. Same as Fig. 7, but for SO_2-based tracer fractions within the 400–420 K layer over the North American continent. The black triangle indicates the location of Boulder.

5 Modelling sensitivities

5.1 ~~Modelling sensitivities~~Sensitivity to parameterized mixing and injection-region definition

To assess the sensitivity of plume dispersion to model settings, such as parameterized mixing intensity, tracer release regions, and release altitudes, we performed a series of sensitivity experiments. In previous work with CLaMS driven by $1° \times 1°$ resolution and ~~6 h~~ 6 hours temporal resolution reanalysis data (e.g., ERA5, ERA-Interim, as applied in Kloss et al. (2021)), the intensity of parameterized small-scale mixing was controlled by choosing a ~~Lyapunov exponent of 1.5~~ critical Lyapunov exponent $\lambda_c = 1.5$ and a mixing ~~frequency of 24 h~~interval of 24 hours (e.g., Pommrich et al. (2014)). Here, we performed simulations with CLaMS driven by high-resolution ERA5 data ($0.3° \times 0.3°$ resolution, ~~1 h~~1 hour) and found best agreement with observations by enhancing mixing intensity in the simulation slightly by choosing ~~a Lyapunov exponent of 3.5~~ $\lambda_c = 3.5$ and a mixing ~~frequency of 6 h.~~ interval of 6 hours. Taken together, the modified setup corresponds to enhanced parameterized mixing compared to the control setup.

To evaluate the sensitivity of our results with respect to ~~small-scale~~ parameterized mixing intensity, Figure A1 in the Appendix shows the SO_2-based tracer fractions from the control simulation (~~Lyapunov = 1.5; mixing = 24 h~~ $\lambda_c = 1.5$; mixing interval $\Delta t = 24$ hours) and compares them with those from the modified simulation (~~Lyapunov = 3.5; mixing = 6 h) in Figure 6.~~ $\lambda_c = 3.5$; $\Delta t = 6$ hours) in Fig. 7. The control simulation in Figure A1 shows a similar overall intrusion pattern but lacks the distinct fractions over Lhasa on 3 August~~.~~ 2019. The tracer distribution in the control simulation is more fragmented, presenting small, isolated pockets compared to the more homogeneous structures in the modified simulation. ~~Note that, for~~ In a further sensitivity test, we repeat the control simulation with ERA5 fields at coarser spatial and temporal resolution (details in Table 2). This setup reduces computing time and is often used for global CLaMS simulations that cover multiple years. However, changing the ~~resolution of the~~ ERA5 ~~driving data~~ resolution has only a minor effect and does not affect our conclusions~~; compare~~. This is evident from the comparison of Fig. A1 ($0.3° \times 0.3°$ ~~resolution~~, 1~~h) with~~ hour) and Fig. A2 ($1° \times 1°$ ~~resolution~~, 6~~h~~ hours).

The ~~SO_2-based tracers from~~ different Raikoke tracers from the global three-dimensional CLaMS simulations are interpolated in time and space to the balloon-borne vertical profiles, providing a tracer-fraction profile at each measurement time. By comparing these tracer-fraction profiles from the model simulations with different mixing intensities with the observations (Fig. ~~7~~9), we assess how the chosen parameterized mixing intensities affect the accuracy of the simulated plume dispersion. To quantify ~~model–measurement~~ model–measurement agreement for each profile, we compute (i) the Pearson correlation coefficient ~~r~~ r between the area-normalized tracer-fraction profile and the COBALD ~~BSR_{455} enhancement (~~aerosol backscatter ratio at 455 nm ($ABSR_{455}$),~~ defined as ~~$BSR_{455} - 1$)~~ $_{455} - 1$ (e.g., Cirisan et al., 2014; Reinares Martínez et al., 2021), over the main plume layer (~~375–450 K; 375–475 K~~ 375–450 K; 375–475 K on 30 September, 28 October, and 24 November~~),~~ 2019) and (ii) the absolute peak-height difference $|\Delta\theta|$ between the two profiles. Note that r reflects only linear association and should be interpreted as a relative indicator rather than a definitive measure of agreement. The values of r and $|\Delta\theta|$ are annotated in Fig. ~~7.~~ 9. In Fig. ~~7~~9, the SO_2-based tracers are also released at 400–420 K. This setup primarily samples the diluted main plume rather than the higher-altitude trailing filament of the vorticized volcanic plume (VVP). Accordingly, the higher-altitude peak on 3 August 2019 likely originates from the VVP filament near 460–490 K and is not resolved by the 400–420 K release.

A sensitivity simulation targeting the upper-level VVP filament shows enhanced tracer fractions near the observation region (not shown here); however, with the currently used CLaMS resolution, this thin and sharp aerosol peak at a single profile location is difficult to reproduce. Consistent with Figures ~~6~~ 7 and A1, the modified simulation produces tracer peaks (blue lines) that closely match the balloon measurements—except on 6 August 2019 and 8 August 2019, when the peak altitudes deviate slightly. For most dates, the modified simulation shows consistently higher r and smaller $|\Delta\theta|$. Although the control simulation (orange lines) occasionally aligns with observed peak altitudes, its overall agreement is weaker and it ~~even generates unexplained extreme values~~ shows large peak-altitude biases on 12 August 2019 and 24 November 2019 ($|\Delta\theta_{\mathrm{peak}}| \approx 25$ K and ≈ 36 K, respectively; Fig. 9). Overall, the modified simulation captures the vertical structure of the BSR_{455} profile well, despite minor differences in peak altitude for certain dates.

Furthermore, we assess the sensitivity of the model simulations to the plume initialization by carrying out another simulation ~~with SO_2-based model tracers~~ using the modified configuration, in which Raikoke plume tracers are initialized within a rectangular latitude–longitude mask (from 163°E to 170°W and 49°N to 62°N), following Kloss et al. (2021) (see Table 2 for simulation details). Tracers were ~~then~~ released on multiple isentropic levels within this rectangular domain. Here, we show the ~~rectangular-mask tracers, calculated by the modified simulation~~rectangle-based tracer fractions, released at potential-temperature levels of 400–420 K ~~during 23–24 June 2019~~ (red lines in Fig. ~~7~~9). The peak heights of the ~~rectangular tracers~~ rectangle-based tracer fractions (red lines) and the SO_2-based ~~tracers~~ tracer fractions (blue lines) show no significant difference. Because the release domain captures the plume core, even a simple rectangular mask reproduces the observed peak altitude. Hence, for the Raikoke simulations the choice of injection region is less critical than the choice of model mixing intensity.

Over Boulder, we likewise compare the ~~model~~ tracer-fraction profiles on the ~~observation~~ measurement dates with the POPS aerosol number concentration profiles at STP (Fig. ~~8~~10). For the computation of r, we evaluate within ~~375–450~~375–450 K for 7 August and 27 August 2019, and within ~~375–475~~375–475 K for 8 November 2019. ~~On 27 August 2019~~Overall, the SO_2-based tracers in the modified simulation (blue) ~~closely~~ reproduce the observed peak ~~. On 7 August 2019, judging by the reproduced peak shape, the SO_2-based tracers from the modified simulation still agree best relative to the SO_2-based tracers in the control simulation and to the rectangular-mask tracers in the modified run.~~ structure more closely, with higher r and smaller $|\Delta\theta|$ than the control and rectangle-based simulations.

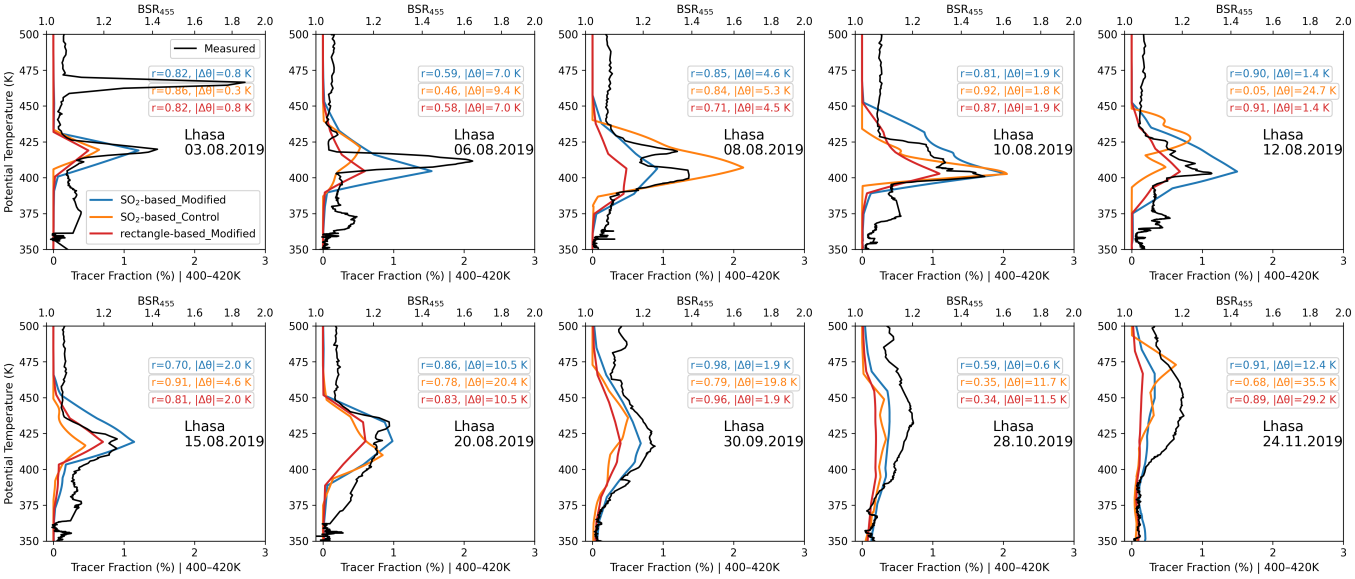

Figure 9. Comparison of ~~tracer-fraction~~ tracer-fraction profiles with the BSR_{455} profile over Lhasa. ~~The labels SO_2-based_Control~~ SO_2-based tracer fractions from the control simulation (orange) and ~~SO_2-based_Modified~~ the modified simulation (blue) ~~denote SO_2-based tracers~~ are shown together with rectangle-based tracer fractions from the ~~control and~~ modified ~~simulations, respectively, while Rectangle_Modified~~ simulation (red)~~denotes tracers from the rectangular release domain in the modified~~ ; see Table 2 for simulation details. Annotation colors match the corresponding simulation profiles. Values give the Pearson correlation r and the absolute peak-height offset $|\Delta\theta|$ (K) between the model tracer-fraction profile and the COBALD $BSR_{~~455~~ 455}$ profile within the analyzed θ range (375–450 K; 375–475 K on 30 September, 28 October, and 24 November 2019).

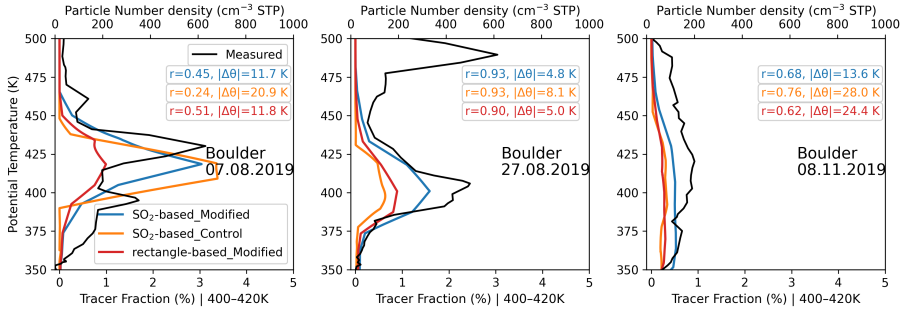

Figure 10. Same as Fig. ~~7~~ 9 but for Boulder: comparison of tracer-fraction profiles with the POPS aerosol number-concentration profile at STP. Annotations report r and $|\Delta\theta|$ (K) relative to POPS within the analyzed θ range (375–450 K for 7 August and 27 August 2019, and 375–475 K for 8 November 2019).

6 ~~Estimation of self-lofting heights~~

5.1 Sensitivity to injection height

The Raikoke plume was injected primarily within 8–16 km (Kloss et al., 2021; Cai et al., 2022; Vernier et al., 2024). The main injection occurred between 18:00 UTC on 21 June and 03:00 UTC on 22 June 2019 (with SO_2 release possibly extending to ~06:00 UTC) (Cai et al., 2022; Vernier et al., 2024). Radiative heating of ash and nascent sulfate then lofted parts of the plume, raising volcanic cloud tops above 20 km within four days of the eruption (Muser et al., 2020; Gorkavyi et al., 2021). These observations indicate that Raikoke's plume experienced an intense updraft during the eruption stage. Aerosol-radiative lofting is not included in the CLaMS simulations. However, comparison of the vertical profiles of the SO_2-based tracers with in-situ measurements allows estimation of the lofting height. SO_2-based tracers were injected at 20 K intervals between 360 K and 500 K to cover the entire possible extent of the Raikoke plume. To assess which initialization range best reproduces the observed plume, we compare tracer-fraction profiles with the BSR_{455} profiles in ~~Figure 9.~~ Fig. 11.

Overall, tracers initialized within 400–420 K (blue lines; ~ 15–16.5 km at the Raikoke site) best match the enhanced BSR_{455} ~~$_{455}$~~ profiles, compared with 380–400 K (brown) and 420–440 K (purple). For most dates, the 400–420 K initialization attains the highest r and the smallest $|\Delta\theta|$ among the three layers (see annotations in Fig. ~~9). In one case, for example on August~~ 11). For instance, on 3~~, August 6 and August~~ August, 6 August, and 12 August 2019, tracers initialized in the 400–420 K layer contribute most strongly to the peak of the BSR_{455} profile, while those from the 380–400 K and 420–440 K layers also produce peaks at the same altitude but with smaller amplitudes. ~~In another case, on~~ On 8 August, 30 September, and 28 October 2019, only the 400–420 K ~~tracers reproduce~~ tracer reproduces the BSR_{455} peak at the correct altitude, whereas the peaks from the 380–400 K and 420–440 K tracers appear below or above the observed height. For Boulder (Fig. ~~10~~12), the 400–420 K initialization likewise shows the best agreement with the observations. On 7 August 2019 the 380–400 K layer, and on 27 August 2019 the 420–440 K layer, produce peaks that disagree strongly with the observations ($r < 0.1$).

~~Based on the Lagrangian reconstruction by Cai et al. (2022), approximately 1.5 Tg of SO_2 was initially injected between about 5 and 15 km, with a peak at around 11 km. If we use this central injection altitude to estimate plume~~ Cai et al. (2022) estimate a peak injection altitude near 11 km, whereas the tracer level that best matches the observed profiles corresponds to ~15–16.5 km (400–420 K). We hypothesize that this ~4–5 km offset could be consistent with radiative self-heating ~~effects, the cloud may then be lofted by an additional ~ 4–5 km. Therefore, the height at which our SO~~lofting of the SO_2 ~~-based tracers best match observations will exceed the true injection center altitude. However, different observational techniques often report varying estimates of the injection center altitude (e.g., Kloss et al., 2021; Cai et al., 2022; Vernier et al., 2024). This also leads to uncertainty in our assessment of radiative lofting heights in this study~~-rich cloud, but it may also reflect uncertainties in injection-height estimates across techniques and model-related discrepancies (e.g., Kloss et al., 2021; Cai et al., 2022; Vernier et al., 2024).

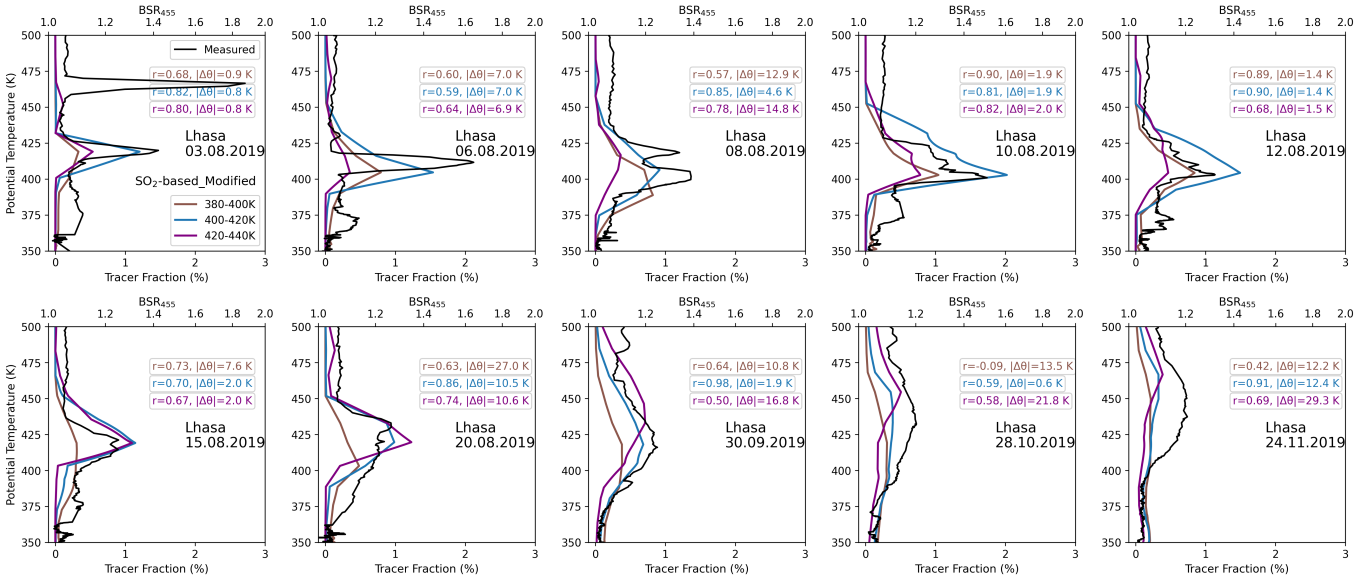

Figure 11. ~~Tracer~~SO_2-based tracer-fraction profiles from the modified simulation at different isentropic injection levels (simulation details in Table 2), compared with COBALD BSR_{455} profiles. Blue lines: injections at 400–420 K; brown lines: 380–400 K; purple lines: 420–440 K. Annotation colors match the corresponding injection-layer curves; values are r and $|\Delta\theta|$ (K) between the model tracer-fraction profile and the COBALD $BSR_{~~455~~}$ $_{455}$ profile within the analyzed θ range (375–450 K; 375–475 K on 30 September, 28 October, and 24 November 2019).

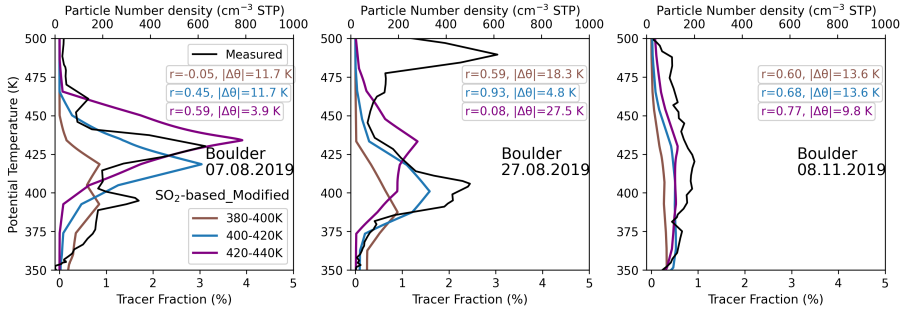

Figure 12. Same as Fig. ~~9~~ 11 but for Boulder: SO_2-based tracer-fraction profiles from the modified simulation at different isentropic injection levels compared with the POPS aerosol number-concentration profile at STP. Blue: 400–420 K; brown: 380–400 K; purple: 420–440 K. Annotations report r and $|\Delta\theta|$ (K) relative to POPS within the analyzed θ range (375–450 K for 7 August 2019 and 27 August 2019, and 375–475 K for 8 November 2019).

6 Conclusions

~~In this study~~Motivated by the limited availability of in-situ UTLS measurements of volcanic plume and the need to better quantify ASMA-related transport pathways, we combined in-situ balloon observations over Lhasa and Boulder with Lagrangian

transport simulations using the CLaMS model, driven by high-resolution ERA5 data, to investigate the transport pathways and mixing processes of the Raikoke plume in the upper troposphere–lower stratosphere (UTLS) during the mature phase of the Asian Summer Monsoon Anticyclone (ASMA). Our main conclusions are:

- **Analysis of backward trajectories.** ~~40~~ 42 days after the Raikoke eruption, the enhanced BSR_{455} was first detected over Lhasa. Two separate transport pathways carried the Raikoke plume to the Tibetan Plateau: (i) a high-altitude pathway along summertime easterly winds ($\sim$ 460–490 K) transporting the trailing filament of the vorticized volcanic plume (VVP) and (ii) a lower-level route via the subtropical westerly jet ($\sim$ 390–430 K) transporting the main volcanic plume. These branches converge over Lhasa on 3 August 2019 but at different altitudes, explaining the dual peaks observed in balloon-borne backscatter profiles.

- **Dilution via mixing with relatively aerosol-poor air.** During ~~stratospheric transport~~ transport through the lower stratosphere, the plume is progressively diluted by background air with low aerosol concentrations. After entering the ASMA, ~~both~~ dilution may be driven by upwelling from lower ~~potential-temperature levels and horizontal entrainment of surrounding aircontribute to this dilution~~potential temperature levels and by dispersion and lateral mixing with surrounding air. These processes are consistent with the progressively smoothed peaks of enhanced BSR_{455} signals observed along the balloon profiles.

- **Validation of CLaMS SO_2-based tracers.** ~~CLaMS modified~~ The modified CLaMS simulations using SO_2-based tracers successfully capture transport into the ASMA and reconstruct the vertical structure observed over Lhasa, as well as over the North American continent in Boulder. Compared with the control simulation (mixing every ~~24 h~~24 hours), the modified simulation (mixing every ~~6 h~~6 hours) produces more coherent tracer distributions that closely match the enhanced BSR_{455} peaks. ~~By comparing SO_2-based tracers released at different isentropic levels, we infer that aerosol-radiative lofting may produce an additional uplift of $\sim$ 4–5 km.~~

In summary, by combining observations and modelling, we provide further insights into how the mid-latitude Raikoke plume is transported ~~, evolves, and spreads out~~ through the Northern Hemisphere UTLS over long distances~~, enters the ASMA, and is progressively diluted.~~. We show evidence that the Asian summer monsoon plays a key role in this transport. In particular, parts of the plume are entrained into the monsoon anticyclone and are subsequently diluted by horizontal transport and vertical upwelling within the anticyclone. Our findings improve the understanding of how aerosols from a mid-latitude volcanic injection are transported and dispersed in the lower stratosphere, including in the vicinity of the Asian summer monsoon. This improved understanding of plume transport and dilution is relevant for estimating regional radiative forcing and assessing potential impacts on stratospheric ozone chemistry.

We identified two distinct isentropic transport pathways and ~~quantified the dilution mechanism via mixing from~~ assessed plume dilution via mixing with air masses outside the plume. Our simulations show that ~~small-scale~~ atmospheric mixing processes, as parameterized in CLaMS in relation to flow deformation, are critical for dispersing the volcanic plume ~~along its pathway through the stratosphere, and that representing these (often subgrid-scale) processes in models is essential for reliable~~

simulations of volcanic plume transport. In this senseduring stratospheric transport. Accordingly, changes in model resolution require adjustment of mixing parameterizations. In particular, our findings show that the ASMA may play an important role in dispersing aerosols from mid-latitude volcanic injections throughout the global stratospherethe mixing parameterization. Our results suggest that a small fraction of the Raikoke plume becomes entrained into the ASMA. Within the ASMA, confinement and summertime diabatic uplift can potentially transport these plume fractions to higher altitudes (e.g., Vogel et al., 2019).

Data availability. Sentinel-5P TROPOMI SO_2 Level-2 OFFL data were obtained from the Copernicus Data Space Ecosystem (last access: 3 June 2025); the product DOI is https://doi.org/10.5270/S5P-74eidii. ERA5 reanalysis was retrieved from the Copernicus Climate Data Store. We used the "ERA5-complete" dataset on the native grid including model levels (https://doi.org/10.24381/cds.143582cf; last access: 3 June 2025). POPS (Baseline Balloon Stratospheric Aerosol Profiles, B^2SAP) 1 Hz time series were downloaded from NOAA CSL (https://csl.noaa.gov/projects/b2sap/data.html, last access: 3 July 2025). Balloon sounding measurements from the SWOP campaign over Lhasa are available upon request from Jianchun Bian (bjc@mail.iap.ac.cn).

Appendix A

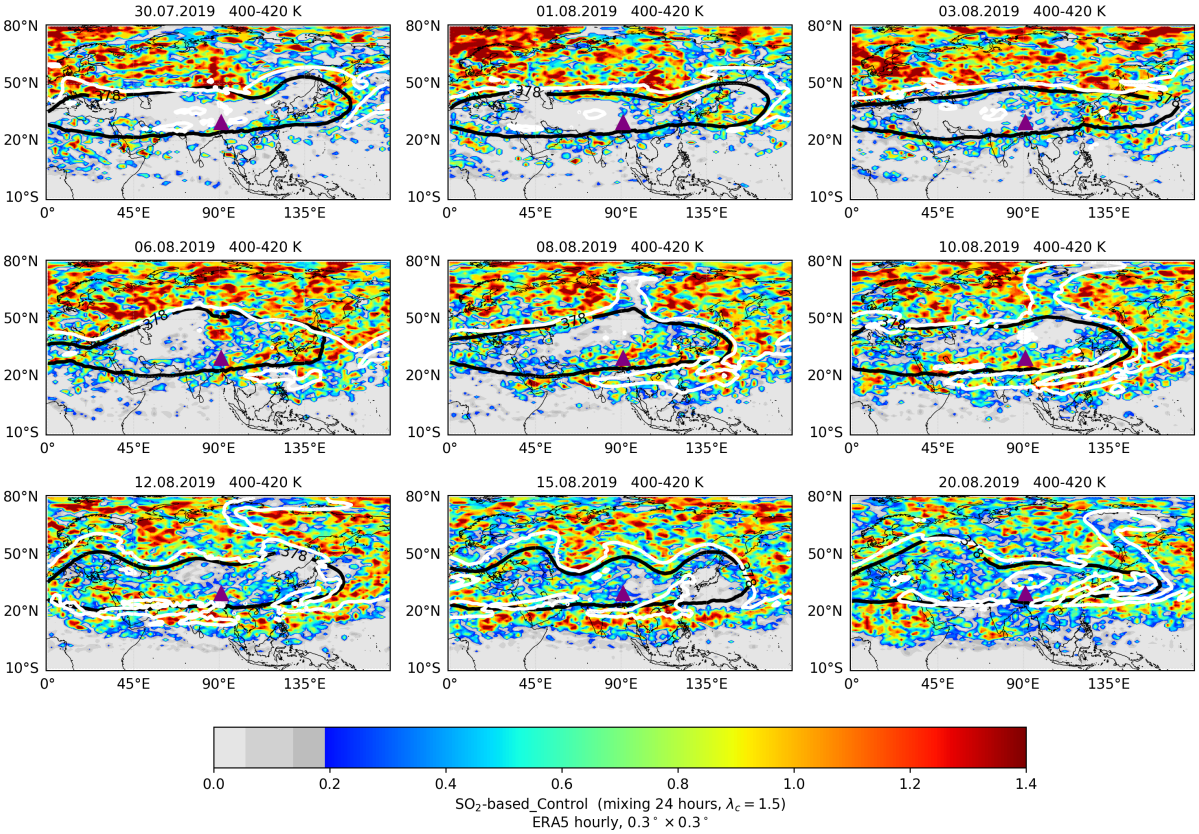

Figure A1. Same as Fig. ~~6~~7, but for SO_2 ~~-based~~ -based tracer fractions from the control simulation ~~for each measurement day~~(simulation details in Table 2), driven by ERA5 at $0.3^\circ \times 0.3^\circ$ spatial and ~~1 h~~ 1 hour temporal resolution.

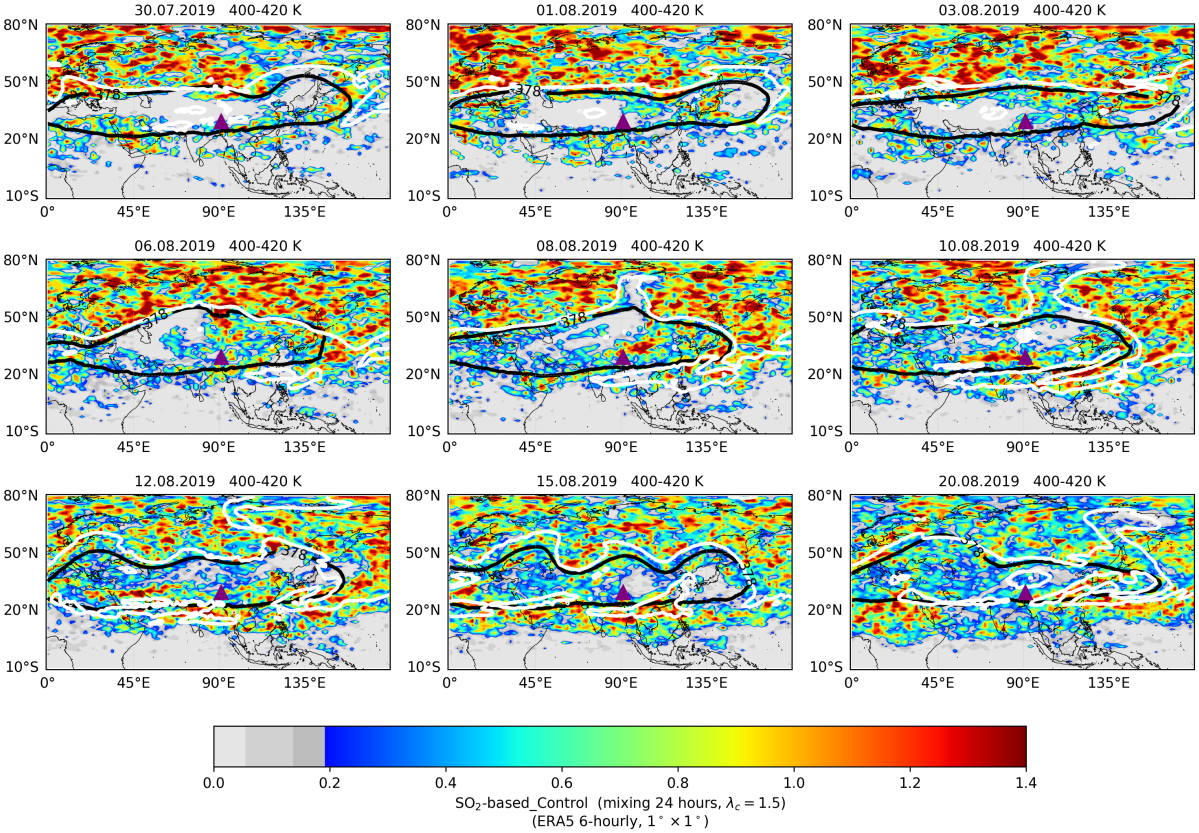

Figure A2. Same as Fig. A1, but driven by ERA5 at $1^\circ \times 1^\circ$ spatial and ~~6 h~~ 6 hours temporal resolution.

Author contributions. ZY, BV, and FP jointly developed the study concept; BV and FP provided the initial idea and scientific guidance throughout; ZY performed the simulations and analyzed the data and results; BV contributed key components of the CLaMS simulation code; FP contributed the CLaMS code for the global three-dimensional tracer simulations; JCB, ZXB, and DL conducted the balloon-borne measurements at Lhasa; SG and LH provided the TROPOMI data; FGW provided technical support for the COBALD instrument/data; EA, AAB, KRS, and TT provided technical support for the POPS data; MIH contributed to the review and editing of the manuscript; ZY wrote the manuscript with input from all co-authors.

Competing interests. The authors declare that they have no competing interests.

Acknowledgements. We thank the three anonymous reviewers for their thorough and constructive reviews.

This research was supported by the Deutsche Forschungsgemeinschaft (DFG grant no. VO 1276/6-1) and the National Natural Science Foundation of China (NSFC Grant 42061134012) in the frame of a joint NSFC-DFG research project as well as by the NSFC Grant 42394121.

We acknowledge the Jülich Supercomputing Centre (JSC; Research Centre Jülich, Germany) for computing time on the supercomputer JUWELS (project CLaMS-ESM) and storage resources on the meteocloud data archive. Further, we thank the European Centre for Medium-Range Weather Forecasts (ECMWF) for providing the ERA5 reanalyses.

Balloon measurements over Boulder are supported by the NOAA cooperative agreement NA22OAR4320151, the Earth Radiation Budget (ERB) project, and the NASA Upper Atmosphere Composition Observations (UACO) program. Katie Smith and Alexandre Baron would like to acknowledge Reflective for supporting this research through their fellowship program.

References

Appel, O., Köllner, F., Dragoneas, A., Hünig, A., Molleker, S., Schlager, H., Mahnke, C., Weigel, R., Port, M., Schulz, C., Drewnick, F., Vogel, B., Stroh, F., and Borrmann, S.: Chemical analysis of the Asian tropopause aerosol layer (ATAL) with emphasis on secondary aerosol particles using aircraft-based in situ aerosol mass spectrometry, Atmos. Chem. Phys., 22, 13 607–13 630, https://doi.org/10.5194/acp-22-13607-2022, 2022.

Bian, J., Pan, L. L., Paulik, L., Vömel, H., and Chen, H.: In situ water vapor and ozone measurements in Lhasa and Kunmin during the Asian summer monsoon, Geophys. Res. Lett., 39, L19808, https://doi.org/10.1029/2012GL052996, 2012.

Bourassa, A. E., Robock, A., Randel, W. J., Deshler, T., Rieger, L. A., Lloyd, N. D., Llewellyn, E., and Degenstein, D. A.: Large volcanic aerosol load in the stratosphere linked to Asian monsoon transport, Science, 337, 78–81, 2012.

Brabec, M., Wienhold, F. G., Luo, B. P., Vömel, H., Immler, F., Steiner, P., Hausammann, E., Weers, U., and Peter, T.: Particle backscatter and relative humidity measured across cirrus clouds and comparison with microphysical cirrus modelling, Atmos. Chem. Phys., 12, 9135–9148, https://doi.org/10.5194/acp-12-9135-2012, 2012.

Brewer, A. W.: Evidence for a world circulation provided by the measurements of helium and water vapour distribution in the stratosphere, Q. J. R. Meteorol. Soc., 75, 351–363, https://doi.org/10.1002/qj.49707532603, 1949.

Brunamonti, S., Jorge, T., Oelsner, P., Hanumanthu, S., Singh, B. B., Kumar, K. R., Sonbawne, S., Meier, S., Singh, D., Wienhold, F. G., Luo, B. P., Boettcher, M., Poltera, Y., Jauhiainen, H., Kayastha, R., Karmacharya, J., Dirksen, R., Naja, M., Rex, M., Fadnavis, S., and Peter, T.: Balloon-borne measurements of temperature, water vapor, ozone and aerosol backscatter on the southern slopes of the Himalayas during StratoClim 2016–2017, Atmos. Chem. Phys., 18, 15 937–15 957, https://doi.org/10.5194/acp-18-15937-2018, 2018.

Brunamonti, S., Martucci, G., Romanens, G., Poltera, Y., Wienhold, F. G., Hervo, M., Haefele, A., and Navas-Guzmán, F.: Validation of aerosol backscatter profiles from Raman lidar and ceilometer using balloon-borne measurements, Atmospheric Chemistry and Physics, 21, 2267–2285, 2021.

Butchart, N.: The Brewer-Dobson circulation, Rev. Geophys., 52, 157–184, https://doi.org/10.1002/2013RG000448, 2014.

Cai, Z., Griessbach, S., and Hoffmann, L.: Improved estimation of volcanic SO_2 injections from satellite retrievals and Lagrangian transport simulations: the 2019 Raikoke eruption, Atmospheric Chemistry and Physics, 22, 6787–6809, https://doi.org/10.5194/acp-22-6787-2022, 2022.

Carn, S., Krotkov, N., Fisher, B., and Li, C.: Out of the blue: Volcanic SO2 emissions during the 2021–2022 eruptions of Hunga Tonga—Hunga Ha'apai (Tonga), Frontiers in Earth Science, 10, 976 962, 2022.

Cirisan, A., Luo, B. P., Engel, I., Wienhold, F. G., Sprenger, M., Krieger, U. K., Weers, U., Romanens, G., Levrat, G., Jeannet, P., Ruffieux, D., Philipona, R., Calpini, B., Spichtinger, P., and Peter, T.: Balloon-borne match measurements of midlatitude cirrus clouds, Atmos. Chem. Phys., 14, 7341–7365, https://doi.org/10.5194/acp-14-7341-2014, 2014.

Clemens, J., Vogel, B., Hoffmann, L., Griessbach, S., Thomas, N., Fadnavis, S., Müller, R., Peter, T., and Ploeger, F.: A multi-scenario Lagrangian trajectory analysis to identify source regions of the Asian tropopause aerosol layer on the Indian subcontinent in August 2016, Atmospheric Chemistry and Physics, 24, 763–787, 2024.

de Leeuw, J., Schmidt, A., Witham, C. S., Theys, N., Taylor, I. A., Grainger, R. G., Pope, R. J., Haywood, J., Osborne, M., and Kristiansen, N. I.: The 2019 Raikoke volcanic eruption – Part 1: Dispersion model simulations and satellite retrievals of volcanic sulfur dioxide, Atmospheric Chemistry and Physics, 21, 10 851–10 879, https://doi.org/10.5194/acp-21-10851-2021, 2021.

Dobson, G. M. B.: Origin and distribution of polyatomic molecules in the atmosphere, Proc R Soc London A, 236, 187–193, 1956.

Fadnavis, S., Schultz, M. G., Semeniuk, K., Mahajan, A. S., Pozzoli, L., Sonbawne, S., Ghude, S. D., Kiefer, M., and Eckert, E.: Trends in peroxyacetyl nitrate (PAN) in the upper troposphere and lower stratosphere over southern Asia during the summer monsoon season: regional impacts, Atmos. Chem. Phys., 14, 12 725–12 743, https://doi.org/10.5194/acp-14-12725-2014, 2014.

Fahey, D. W., Gao, R.-S., Möhler, O., Saathoff, H., Schiller, C., Ebert, V., Krämer, M., Peter, T., Amarouche, N., Avallone, L. M., Bauer, R., Bozóki, Z., Christensen, L. E., Davis, S. M., Durry, G., Dyroff, C., Herman, R. L., Hunsmann, S., Khaykin, S. M., Mackrodt, P., Meyer, J., Smith, J. B., Spelten, N., Troy, R. F., Vömel, H., Wagner, S., and Wienhold, F. G.: The AquaVIT-1 intercomparison of atmospheric water vapor measurement techniques, Atmos. Meas. Tech., 7, 3177–3213, https://doi.org/10.5194/amt-7-3177-2014, 2014.

Fromm, M., Nedoluha, G., and Charvát, Z.: Comment on "Large Volcanic Aerosol Load in the Stratosphere Linked to Asian Monsoon Transport", Science, 339, 647, https://doi.org/10.1126/science.1228605, 2013.

Gao, R. S., Telg, H., McLaughlin, R. J., Ciciora, S. J., Watts, L. A., Richardson, M. S., Schwarz, J. P., Perring, A. E., Thornberry, T. D., Rollins, A. W., Markovic, M. Z., Bates, T. S., Johnson, J. E., and Fahey, D. W.: A light-weight, high-sensitivity particle spectrometer for PM2.5 aerosol measurements, Aerosol Science and Technology, 50, 88–99, https://doi.org/10.1080/02786826.2015.1131809, 2016.

Gorkavyi, N., Krotkov, N., Li, C., Lait, L., Colarco, P., Carn, S., DeLand, M., Newman, P., Schoeberl, M., Taha, G., Torres, O., Vasilkov, A., and Joiner, J.: Tracking aerosols and SO_2 clouds from the Raikoke eruption: 3D view from satellite observations, Atmospheric Measurement Techniques, 14, 7545–7563, https://doi.org/10.5194/amt-14-7545-2021, 2021.

GRUAN Lead Centre: InterMet iMet-1 (iMet-1-RSB) — GRUAN instrument information (radiosonde models), https://www.gruan.org/instruments/radiosondes/sonde-models/intermet-imet-1, accessed 13 Jan 2026, 2025.

Hanumanthu, S., Vogel, B., Müller, R., Brunamonti, S., Fadnavis, S., Li, D., Ölsner, P., Naja, M., Singh, B. B., Kumar, K. R., Sonbawne, S., Jauhiainen, H., Vömel, H., Luo, B., Jorge, T., Wienhold, F. G., Dirkson, R., and Peter, T.: Strong day-to-day variability of the Asian Tropopause Aerosol Layer (ATAL) in August 2016 at the Himalayan foothills, Atmos. Chem. Phys., 20, 14 273–14 302, https://doi.org/10.5194/acp-20-14273-2020, 2020.

He, Y., Jing, D., Yin, Z., Ohneiser, K., and Yi, F.: Long-term (2010–2021) lidar observations of stratospheric aerosols in Wuhan, China, Atmospheric Chemistry and Physics, 24, 11 431–11 450, 2024.

Hersbach, H., Bell, B., Berrisford, P., Hirahara, S., Horànyi, A., Muñoz Sabater, J., Nicolas, J., Peubey, C., Radu, R., Schepers, D., Simmons, A., Soci, C., Abdalla, S., Abellan, X., Balsamo, G., Bechtold, P., Biavati, G., Bidlot, J., Bonavita, M., De Chiara, G., Dahlgren, P., Dee, D., Diamantakis, M., Dragani, R., Flemming, J., Forbes, R., Fuentes, M., Geer, A., Haimberger, L., Healy, S., Hogan, R. J., Hólm, E., Janisková, M., Keeley, S., Laloyaux, P., Lopez, P., Lupu, C., Radnoti, G., de Rosnay, P., Rozum, I., Vamborg, F., Villaume, S., and Thépaut, J.-N.: The ERA5 global reanalysis, Q. J. R. Meteorol. Soc., 146, 1999–2049, https://doi.org/10.1002/qj.3803, 2020.

Hoffmann, L., Günther, G., Li, D., Stein, O., Wu, X., Griessbach, S., Heng, Y., Konopka, P., Müller, R., Vogel, B., and Wright, J. S.: From ERA-Interim to ERA5: the considerable impact of ECMWF's next-generation reanalysis on Lagrangian transport simulations, Atmos. Chem. Phys., 19, 3097–3124, https://doi.org/10.5194/acp-19-3097-2019, 2019.

Hofmann, D. J. and Solomon, S.: Ozone destruction through heterogeneous chemistry following the eruption of El Chichón, J. Geophys. Res., 94, 5029–5041, 1989.

Jing, D., He, Y., Yin, Z., Liu, F., Yi, Y., and Yi, F.: Evolution of aerosol plumes from 2019 Raikoke volcanic eruption observed with polarization lidar over central China, Atmospheric Environment, 309, 119 880, 2023.

Khaykin, S. M., De Laat, A. J., Godin-Beekmann, S., Hauchecorne, A., and Ratynski, M.: Unexpected self-lofting and dynamical confinement of volcanic plumes: the Raikoke 2019 case, Scientific Reports, 12, 22 409, 2022.

Kloss, C., Berthet, G., Sellitto, P., Ploeger, F., Taha, G., Tidiga, M., Eremenko, M., Bossolasco, A., Jégou, F., Renard, J.-B., and Legras, B.: Stratospheric aerosol layer perturbation caused by the 2019 Raikoke and Ulawun eruptions and their radiative forcing, Atmospheric Chemistry and Physics, 21, 535–560, https://doi.org/10.5194/acp-21-535-2021, 2021.

Konopka, P., Steinhorst, H.-M., Grooß, J.-U., Günther, G., Müller, R., Elkins, J. W., Jost, H.-J., Richard, E., Schmidt, U., Toon, G., and McKenna, D. S.: Mixing and Ozone Loss in the 1999-2000 Arctic Vortex: Simulations with the 3-dimensional Chemical Lagrangian Model of the Stratosphere (CLaMS), J. Geophys. Res., 109, D02315, https://doi.org/10.1029/2003JD003792, 2004.

Konopka, P., Günther, G., Müller, R., dos Santos, F. H. S., Schiller, C., Ravegnani, F., Ulanovsky, A., Schlager, H., Volk, C. M., Viciani, S., Pan, L. L., McKenna, D.-S., and Riese, M.: Contribution of mixing to upward transport across the tropical tropopause layer (TTL), Atmos. Chem. Phys., 7, 3285–3308, 2007.

Konopka, P., Grooß, J.-U., Plöger, F., and Müller, R.: Annual cycle of horizontal in-mixing into the lower tropical stratosphere, J. Geophys. Res., 114, D19111, https://doi.org/10.1029/2009JD011955, 2009.

Li, D., Vogel, B., Bian, J., Müller, R., Pan, L. L., Günther, G., Bai, Z., Li, Q., Zhang, J., Fan, Q., and Vömel, H.: Impact of typhoons on the composition of the upper troposphere within the Asian summer monsoon anticyclone: the SWOP campaign in Lhasa 2013, Atmos. Chem. Phys., 17, 4657–4672, 2017.

Li, D., Vogel, B., Müller, R., Bian, J., Günther, G., Li, Q., Zhang, J., Bai, Z., Vömel, H., and Riese, M.: High tropospheric ozone in Lhasa within the Asian summer monsoon anticyclone in 2013: influence of convective transport and stratospheric intrusions, Atmos. Chem. Phys., 18, 17 979–17 994, https://doi.org/10.5194/acp-18-17979-2018, 2018.

Li, D., Vogel, B., Müller, R., Bian, J., Günther, G., Ploeger, F., Li, Q., Zhang, J., Bai, Z., Vömel, H., and Riese, M.: Dehydration and low ozone in the tropopause layer over the Asian monsoon caused by tropical cyclones: Lagrangian transport calculations using ERA-Interim and ERA5 reanalysis data, Atmos. Chem. Phys., 20, 4133–4152, https://doi.org/10.5194/acp-20-4133-2020, 2020.

Ma, D., Bian, J., Li, D., Bai, Z., Li, Q., Zhang, J., Wang, H., Zheng, X., Hurst, D. F., and Vömel, H.: Mixing characteristics within the tropopause transition layer over the Asian summer monsoon region based on ozone and water vapor sounding data, Atmospheric Research, 271, 106 093, 2022.

Masson-Delmotte, V., Zhai, P., Pirani, A., Connors, S. L., Péan, C., Berger, S., Caud, N., Chen, Y., Goldfarb, L., Gomis, M. I., Huang, M., Leitzell, K., Lonnoy, E., Matthews, J. B. R., Maycock, T. K., Waterfield, T., Yelekçi, O., Yu, R., and Zhou, B., eds.: Climate Change 2021: The Physical Science Basis, Cambridge University Press, Cambridge, United Kingdom and New York, NY, USA, https://doi.org/10.1017/9781009157896, 2021.

McCormick, M. P., Thomason, L. W., and Trepte, C. R.: Atmospheric effects of the Mt Pinatubo eruption, Nature, 373, 399–404, 1995.

McKenna, D. S., Konopka, P., Grooß, J.-U., Günther, G., Müller, R., Spang, R., Offermann, D., and Orsolini, Y.: A new Chemical Lagrangian Model of the Stratosphere (CLaMS): 1. Formulation of advection and mixing, J. Geophys. Res., 107, 4309, https://doi.org/10.1029/2000JD000114, 2002.

Mei, F., McMeeking, G., Pekour, M., Gao, R.-S., Kulkarni, G., China, S., Telg, H., Dexheimer, D., Tomlinson, J., and Schmid, B.: Performance assessment of portable optical particle spectrometer (Pops), Sensors, 20, 6294, 2020.

Minnis, P., Harrison, E., Stowe, L., Gibson, G., Denn, F., Doelling, D., and Smith Jr, W.: Radiative climate forcing by the Mount Pinatubo eruption, Science, 259, 1411–1415, 1993.

Murphy, D. M. and Koop, T.: Review of the vapour pressures of ice and supercooled water for atmospheric applications, qjrms, 131, 1539–1565, 2005.

Muser, L. O., Hoshyaripour, G. A., Bruckert, J., Horváth, Á., Malinina, E., Wallis, S., Prata, F. J., Rozanov, A., von Savigny, C., Vogel, H., et al.: Particle aging and aerosol–radiation interaction affect volcanic plume dispersion: evidence from the Raikoke 2019 eruption, Atmospheric Chemistry and Physics, 20, 15 015–15 036, 2020.

Newhall, C. G. and Self, S.: The volcanic explosivity index (VEI) an estimate of explosive magnitude for historical volcanism, Journal of Geophysical Research: Oceans, 87, 1231–1238, 1982.

Park, M., Randel, W. J., Gettleman, A., Massie, S. T., and Jiang, J. H.: Transport above the Asian summer monsoon anticyclone inferred from Aura Microwave Limb Sounder tracers, J. Geophys. Res., 112, D16309, https://doi.org/10.1029/2006JD008294, 2007.

Ploeger, F., Gottschling, C., Grießbach, S., Grooß, J.-U., Günther, G., Konopka, P., Müller, R., Riese, M., Stroh, F., Tao, M., Ungermann, J., Vogel, B., and von Hobe, M.: A potential vorticity-based determination of the transport barrier in the Asian summer monsoon anticyclone, Atmos. Chem. Phys., 15, 13 145–13 159, https://doi.org/10.5194/acp-15-13145-2015, 2015.

Ploeger, F., Diallo, M., Charlesworth, E., Konopka, P., Legras, B., Laube, J. C., Grooß, J.-U., Günther, G., Engel, A., and Riese, M.: The stratospheric Brewer–Dobson circulation inferred from age of air in the ERA5 reanalysis, Atmos. Chem. Phys., 21, 8393–8412, https://doi.org/10.5194/acp-21-8393-2021, 2021.

Poltera, Y., Luo, B., Wienhold, F. G., and Peter, T.: The “Golden Points” and nonequilibrium correction of high-accuracy frost point hygrometers, EGUsphere, 2025, 1–64, 2025.

Pommrich, R., Müller, R., Grooß, J.-U., Konopka, P., Ploeger, F., Vogel, B., Tao, M., Hoppe, C. M., Günther, G., Spelten, N., Hoffmann, L., Pumphrey, H.-C., Viciani, S., D’Amato, F., Volk, C. M., Hoor, P., Schlager, H., and Riese, M.: Tropical troposphere to stratosphere transport of carbon monoxide and long-lived trace species in the Chemical Lagrangian Model of the Stratosphere (CLaMS), Geosci. Model Dev., 7, 2895–2916, https://doi.org/10.5194/gmd-7-2895-2014, 2014.

Portmann, R. W., Solomon, S., Garcia, R. R., Thomason, L. W., Poole, L. R., and McCormick, M. P.: Role of aerosol variations in anthropogenic ozone depletion in the polar regions, J. Geophys. Res., 101, 22 991–23 006, 1996.

Randel, W. J., Park, M., Emmons, L., Kinnison, D., Bernath, P., Walker, K. A., Boone, C., and Pumphrey, H.: Asian Monsoon Transport of Pollution to the Stratosphere, Science, 328, 611–613, https://doi.org/10.1126/science.1182274, 2010.

Reinares Martínez, I., Evan, S., Wienhold, F., Brioude, J., Jensen, E., Thornberry, T., Héron, D., Verreyken, B., Körner, S., Vömel, H., et al.: Unprecedented observations of a nascent in situ cirrus in the tropical tropopause layer, Geophysical Research Letters, 48, e2020GL090 936, 2021.

Santee, M. L., Manney, G. L., Livesey, N. J., Schwartz, M. J., Neu, J. L., and Read, W. G.: A comprehensive overview of the climatological composition of the Asian summer monsoon anticyclone based on 10 years of Aura Microwave Limb Sounder measurements, J. Geophys. Res., 122, 5491–5514, https://doi.org/10.1002/2016JD026408, 2017.

Schmidt, A. and Black, B. A.: Reckoning with the rocky relationship between eruption size and climate response: toward a volcano-climate index, Annual Review of Earth and Planetary Sciences, 50, 627–661, 2022.

Schmidt, A., Mills, M. J., Ghan, S., Gregory, J. M., Allan, R. P., Andrews, T., Bardeen, C. G., Conley, A., Forster, P. M., Gettelman, A., et al.: Volcanic radiative forcing from 1979 to 2015, Journal of Geophysical Research: Atmospheres, 123, 12 491–12 508, 2018.

Solomon, S.: Stratospheric ozone depletion: A review of concepts and history, Rev. Geophys., 37, 275–316, https://doi.org/10.1029/1999RG900008, 1999.

Solomon, S., Daniel, J. S., Neely, R. R., Vernier, J.-P., Dutton, E. G., and Thomason, L. W.: The Persistently Variable “Background” Stratospheric Aerosol Layer and Global Climate Change, Science, 333, 866–870, https://doi.org/10.1126/science.1206027, 2011.

Solomon, S., Ivy, D. J., Kinnison, D., Mills, M. J., Neely, R. R., and Schmidt, A.: Emergence of healing in the Antarctic ozone layer, Science, 353, 269–274, https://doi.org/10.1126/science.aae0061, 2016.

Tabazadeh, A., Drdla, K., Schoeberl, M. R., Hamill, P., and Toon, O. B.: Arctic "ozone hole" in a cold volcanic stratosphere, Proc. Natl. Acad. Sci., 99, 2609–2612, 2002.

Theys, N., De Smedt, I., Yu, H., Danckaert, T., van Gent, J., Hörmann, C., Wagner, T., Hedelt, P., Bauer, H., Romahn, F., et al.: Sulfur dioxide retrievals from TROPOMI onboard Sentinel-5 Precursor: algorithm theoretical basis, Atmospheric Measurement Techniques, 10, 119–153, 2017.

Theys, N., Smedt, I. D., Lerot, C., Vlietinck, J., Yu, H., Roozendael, M. V., Hedelt, P., and Romahn, F.: Sentinel-5P/TROPOMI SO_2 Level-2 Algorithm Theoretical Basis Document, https://sentinels.copernicus.eu/documents/247904/2476257/Sentinel-5P-ATBD-SO2-TROPOMI.pdf, 87 pp., 2024.

Thompson, D. W. J. and Solomon, S.: Understanding Recent Stratospheric Climate Change, Journal of Climate, 22, 1934 – 1943, https://doi.org/10.1175/2008JCLI2482.1, 2009.

Todt, M. A., Asher, E., Hall, E., Cullis, P., Jordan, A., Xiong, K., Hurst, D. F., and Thornberry, T.: Baseline Balloon Stratospheric Aerosol Profiles (B2SAP)—Systematic Measurements of Aerosol Number Density and Size, Journal of Geophysical Research: Atmospheres, 128, e2022JD038 041, https://doi.org/https://doi.org/10.1029/2022JD038041, e2022JD038041 2022JD038041, 2023.

Toohey, M., Jia, Y., Khanal, S., and Tegtmeier, S.: Stratospheric residence time and the lifetime of volcanic stratospheric aerosols, Atmospheric Chemistry and Physics, 25, 3821–3839, 2025.

Veefkind, J. P., Aben, I., McMullan, K., Förster, H., De Vries, J., Otter, G., Claas, J., Eskes, H., De Haan, J., Kleipool, Q., et al.: TROPOMI on the ESA Sentinel-5 Precursor: A GMES mission for global observations of the atmospheric composition for climate, air quality and ozone layer applications, Remote sensing of environment, 120, 70–83, 2012.

Vernier, J., Thomason, L. W., Fairlie, T. D., Minnis, P., Bedka, K. M., and Palikonda, R.: Comment on "Large Volcanic Aerosol Load in the Stratosphere Linked to Asian Monsoon Transport", Science, 339, 647, https://doi.org/10.1126/science.1227817, 2013.

Vernier, J. P., Fairlie, T. D., Natarajan, M., Wienhold, F. G., Bian, J., Martinsson, B. G., Crumeyrolle, S., Thomason, L. W., and Bedka, K. M.: Increase in upper tropospheric and lower stratospheric aerosol levels and its potential connection with Asian pollution, J. Geophys. Res., 120, 1608–1619, https://doi.org/10.1002/2014JD022372, 2015.

Vernier, J.-P., Fairlie, T. D., Deshler, T., Ratnam, M. V., Gadhavi, H., Kumar, B. S., Natarajan, M., Pandit, A. K., Raj, S. T. A., Kumar, A. H., Jayaraman, A., Singh, A. K., Rastogi, N., Sinha, P. R., Kumar, S., Tiwari, S., Wegner, T., Baker, N., Vignelles, D., Stenchikov, G., Shevchenko, I., Smith, J., Bedka, K., Kesarkar, A., Singh, V., Bhate, J., Ravikiran, V., Rao, M. D., Ravindrababu, S., Patel, A., Vernier, H., Wienhold, F. G., Liu, H., Knepp, T. N., Thomason, L., Crawford, J., Ziemba, L., Moore, J., Crumeyrolle, S., Williamson, M., Berthet, G., Jégou, F., and Renard, J.-B.: BATAL: The Balloon Measurement Campaigns of the Asian Tropopause Aerosol Layer, Bull. Am. Meteorol. Soc., 99, 955–973, https://doi.org/10.1175/BAMS-D-17-0014.1, 2018.

Vernier, J.-P., Aubry, T. J., Timmreck, C., Schmidt, A., Clarisse, L., Prata, F., Theys, N., Prata, A. T., Mann, G., Choi, H., et al.: The 2019 Raikoke eruption as a testbed used by the Volcano Response group for rapid assessment of volcanic atmospheric impacts, Atmospheric Chemistry and Physics, 24, 5765–5782, 2024.

Vogel, B., Günther, G., Müller, R., Grooß, J.-U., Afchine, A., Bozem, H., Hoor, P., Krämer, M., Müller, S., Riese, M., Rolf, C., Spelten, N., Stiller, G. P., Ungermann, J., and Zahn, A.: Long-range transport pathways of tropospheric source gases originating in Asia into the northern lower stratosphere during the Asian monsoon season 2012, Atmos. Chem. Phys., 16, 15 301–15 325, https://doi.org/10.5194/acp-16-15301-2016, 2016.

Vogel, B., Müller, R., Günther, G., Spang, R., Hanumanthu, S., Li, D., Riese, M., and Stiller, G. P.: Lagrangian simulations of the transport of young air masses to the top of the Asian monsoon anticyclone and into the tropical pipe, Atmos. Chem. Phys., 19, 6007–6034, https://doi.org/10.5194/acp-19-6007-2019, 2019.

Vogel, B., Volk, C. M., Wintel, J., Lauther, V., Clemens, J., Grooß, J.-U., Günther, G., Hoffmann, L., Laube, J. C., Müller, R., et al.: Evaluation of vertical transport in ERA5 and ERA-Interim reanalysis using high-altitude aircraft measurements in the Asian summer monsoon 2017, Atmospheric Chemistry and Physics, 24, 317–343, 2024.

Vogel, B., Lauther, V., Köllner, F., Ekinci, F., Rolf, C., Strobel, J., van Luijt, R., Volk, M. C., Borrmann, S., Dragoneas, A., Eppers, O., Molleker, S., Hoor, P., Ort, L., Weyland, F., Zahn, A., Clemens, J., Günther, G., Kachula, O., Müller, R., Ploeger, F., and Riese, M.: Continental and marine source regions contributing to the outflow of the Asian summer monsoon anticyclone during the PHILEAS campaign in summer 2023, EGUsphere, 2025, 1–49, https://doi.org/10.5194/egusphere-2025-5609, 2025.

Vömel, H., Naebert, T., Dirksen, R., and Sommer, M.: An update on the uncertainties of water vapor measurements using cryogenic frost point hygrometers, Atmos. Meas. Tech., 9, 3755–3768, https://doi.org/10.5194/amt-9-3755-2016, 2016.

Wu, X., Qiao, Q., Chen, B., Wang, X., Hoffmann, L., Griessbach, S., Tian, Y., and Wang, Y.: The influence of the Asian summer monsoon on volcanic aerosol transport in the UTLS region, npj Climate and Atmospheric Science, 6, 11, 2023.

Yang, Z., Li, D., Luo, J., Tian, W., Bai, Z., Li, Q., Zhang, J., Wang, H., Zheng, X., Vömel, H., et al.: Determination of cirrus occurrence and distribution characteristics over the Tibetan Plateau based on the SWOP campaign, Journal of Geophysical Research: Atmospheres, 128, e2022JD037 682, 2023.

Yu, P., Rosenlof, K. H., Liu, S., Telg, H., Thornberry, T. D., Rollins, A. W., Portmann, R. W., Bai, Z., Ray, E. A., Duan, Y., Pan, L. L., Toon, O. B., Bian, J., and Gao, R.-S.: Efficient transport of tropospheric aerosol into the stratosphere via the Asian summer monsoon anticyclone, Proc. Natl. Acad. Sci., 114, 6972–6977, https://doi.org/10.1073/pnas.1701170114, 2017.

Yu, P., Portmann, R. W., Peng, Y., Liu, C.-C., Zhu, Y., Asher, E., Bai, Z., Lu, Y., Bian, J., Mills, M., et al.: Radiative forcing from the 2014–2022 volcanic and wildfire injections, Geophysical Research Letters, 50, e2023GL103 791, 2023.

Zhu, Y., Bardeen, C. G., Tilmes, S., Mills, M. J., Wang, X., Harvey, V. L., Taha, G., Kinnison, D., Portmann, R. W., Yu, P., et al.: Perturbations in stratospheric aerosol evolution due to the water-rich plume of the 2022 Hunga-Tonga eruption, Communications Earth & Environment, 3, 248, 2022.

Zuev, V., Zueva, N., Savelieva, E., and Gerasimov, V.: The Antarctic ozone depletion caused by Erebus volcano gas emissions, Atmospheric Environment, 122, 393–399, https://doi.org/https://doi.org/10.1016/j.atmosenv.2015.10.005, 2015.